Supporting Information

Impact of urban pollution on organic-mediated new particle formation and particle number concentration in the Amazon rainforest

Bin Zhao[*,†], *Jerome D. Fast*[†], *Neil M. Donahue*[‡,§,||,⊥], *Manish Shrivastava*[†], *Meredith Schervish*[‡,§], *John E. Shilling*[†], *Hamish Gordon*[‡], *Jian Wang*[#], *Yang Gao*[▽], *Rahul A. Zaveri*[†], *Ying Liu*[†], *Brian Gaudet*[†]

[†]Pacific Northwest National Laboratory, Richland, Washington, USA

[‡]Center for Atmospheric Particle Studies, Carnegie Mellon University, Pittsburgh, PA 15213, USA

[§]Department of Chemistry, Carnegie Mellon University, Pittsburgh, PA 15213, USA

[||]Department of Engineering and Public Policy, Carnegie Mellon University, Pittsburgh, PA 15213, USA

[⊥]Department of Chemical Engineering, Carnegie Mellon University, Pittsburgh, PA 15213, USA

[#]Center for Aerosol Science and Engineering, Department of Energy, Environmental and Chemical Engineering, Washington University in St. Louis, Missouri, USA

[▽]Key Laboratory of Marine Environment and Ecology, Ministry of Education/Institute for Advanced Ocean Study, Ocean University of China, Qingdao 266100, China

***Corresponding Author**

Bin Zhao Phone: +1-3109231612; e-mail: bin.zhao@pnnl.gov.

Number of pages: 36

Number of tables: 3

Number of figures: 13

1. More details of the model and its configuration

The parameterizations of NPF rates were developed in several previous studies based on experiments in the CLOUD (Cosmics Leaving Outdoor Droplets) chamber,[1-4] with a couple of updates in our previous study.[5] The NPF rates at 1.7 nm mobility equivalent diameter are calculated as the sum of the following parametrizations:

(1) Binary neutral (indicated by *b*, *n*) and ion-induced (*b*, *i*) NPF involving sulfuric acid:

$$J_{SA} = k_{b,n}(T)[H_2SO_4]^{p_{b,n}} + k_{b,i}(T)[H_2SO_4]^{p_{b,i}}[n_-]$$

where the $k(T)$ is a temperature-dependent prefactor and includes free-fitting parameters (see equations below), *p* is a constant free parameter, and $[n_-]$ is the concentration of negative ions.

(2) Ternary neutral (indicated by *t*, *n*) and ion-induced (*t*, *i*) NPF involving sulfuric acid and NH_3:

$$J_{SA,NH3} = k_{t,n}(T)f_n([NH_3],[H_2SO_4])[H_2SO_4]^{p_{t,n}} + k_{t,i}(T)f_i([NH_3],[H_2SO_4])[H_2SO_4]^{p_{t,i}}[n_-]$$

where the $f([NH_3],[H_2SO_4])$ is a function of the ammonia and sulfuric acid concentrations, also involving free-fitting parameters.

All the $k(T)$ in (1) and (2), for temperatures T in Kelvin, are given by:

$$\ln k_{(x,y)} = u_{(x,y)} - \exp\left(v_{(x,y)}\left(T/1000 - w_{(x,y)}\right)\right)$$

where *x* = *b* or *t* (binary and ternary) and *y* = *n* or *i* (neutral and ion-induced). The functions $f_y([NH_3],[H_2SO_4])$ are

$$f_y([NH_3],[H_2SO_4]) = [NH_3]/\left(a_y + [H_2SO_4]^{p_{t,y}}/[NH_3]^{p_{A,y}}\right)$$

(3) NPF of organics with sulfuric acid:

$$J_{SA-org} = k_{SA-org}[H_2SO_4]^2(33.0 \times 0.667[ELVOC_{O:C>0.4}])$$

where $[ELVOC_{O:C>0.4}]$ refers to the concentration of ELVOC with O:C >0.4 from the oxidation of monoterpenes, and k_{SA-org} is a fitted parameter. The factor 0.667 corrects for the large yield

of ELVOC from α-pinene (a type of endocyclic monoterpene) compared to other monoterpenes, as endocyclic monoterpenes comprise nearly 2/3 of all monoterpene emissions over the Amazon.[6] The adjustment factor of 33.0 is the ratio of total monoterpene oxidation products to ELVOC with O:C >0.4 under the environmental conditions where the parameterizations were developed.[5]

(4) NPF from organics alone, a sum of neutral ($J_{n,org}$) and ion-induced ($J_{iin,org}$) components:

$$J_{n,org} = a_1(3.6 \times 0.667[ULVOC_{O:C>0.4}])^{a_2+a_5/(3.6\times0.667[ULVOC_{O:C>0.4}])}$$

$$J_{iin,org} = a_3(3.6 \times 0.667[ULVOC_{O:C>0.4}])^{a_4+a_5/(3.6\times0.667[ULVOC_{O:C>0.4}])}[n_{\pm}]$$

where $[ULVOC_{O:C>0.4}]$ refers to the concentration of ULVOC with O:C >0.4 from the oxidation of monoterpenes and is given here for convenience in units of 10^7 molecules cm^{-3}, $[n_{\pm}]$ is the ion concentration (equal to $[n_-]$, but ions of both signs participate in this NPF process), and a_i are free parameters. The factor 0.667 has the same meaning as described above. The adjustment factor of 3.6 is the ratio of highly oxygenated organic molecules (HOMs) to ULVOC with O:C >0.4 under the environmental conditions where the parameterizations were developed.[5]

(5) In a sensitivity simulation, we also consider the NPF of H_2SO_4 with amines. Assuming all amines nucleate at the same rate as dimethylamine (DMA), the NPF rate is given by:

$$J_{SA-Amine} = k_{SA-Amine-1}\left([DMA]/(2.5 \times 10^7)\right)[H_2SO_4]^{3.7}$$

for $[DMA] > 2\times10^8$ cm^{-3}, and

$$J_{SA-Amine} = k_{SA-Amine-}\left([DMA]/(2.5 \times 10^7)\right)^{4.36}[H_2SO_4]^{3.7}$$

for $[DMA] < 2\times10^8$ cm^{-3}. $k_{SA-Amine-1}$ and $k_{SA-Amine-}$ are fitted parameters.

The values of all parameters in the equations above are given in Table S1 (shown below). Attention must be paid to the units of the gas concentrations, specified in the table footnotes.

The parameterizations above do not consider the impact of relative humidity on organic-mediated NPF. It is not easy to investigate the impact of relative humidity on NPF during the wet

season of the Amazon based on available observational data because the relative humidity is almost always quite high in the boundary layer—the region this study focuses on and most observational data are available in. The relative humidity within our domain is as high as 89.6±11.6% at the surface level and 87.5±9.2 at 500 m height during our simulation period (Table S3). From the laboratory perspective, Li et al.[7] investigated the effect of relative humidity on the formation of highly oxygenated organic molecules and new particles in a flow tube reactor. They found that as relative humidity increases from ~3% to ~92%, the total SOA number concentrations decrease by a factor of 2–3, suggesting that high RH might inhibit pure-organic NPF. However, the mechanisms for this inhibition remain unclear. Also, the conclusion derived from pure-organic NPF by Li et al.[7] may not be directly applicable to the NPF of H_2SO_4 with organics—the main NPF pathway in our region of interest. Besides, since the relative humidity in the wet season of the Amazon has a relatively small variability, the effect of relative humidity on NPF in this region is expected to be smaller than the effect shown by Li et al.[7] Because of these reasons, we do not consider the effect of relative humidity on organic-mediated NPF in our model. We are interested in considering this effect when more quantitative and mechanistic experimental evidence becomes available.

As described in the main text, we use the MOSAIC (Model for Simulating Aerosol Interaction and Chemistry) aerosol module[8] in our simulation. We changed the accommodation coefficient for the condensation of H_2SO_4 from 0.1 in the original MOSAIC module to 1.0, following Hanson[9]. The aqueous-phase chemistry is based on the Carnegie Mellon University (CMU) scheme of Fahey and Pandis[10]. The biogenic emissions are calculated online using the Model of Emissions of Gases and Aerosols from Nature (MEGAN v2.1)[11] that has been recently coupled within the land surface scheme CLM4 in WRF-Chem.[12] We reduce the monoterpene emissions predicted by MEGAN

v2.1 by a factor of 2 so that the simulated magnitude of monoterpene concentrations generally agrees with aircraft observations (see the main text). A previous modeling study over the Amazon also suggested that the simulated monoterpene concentrations using MEGAN v2.1 overpredicted observations by about a factor of 2.[13] The vertical resolution of the simulation includes 45 layers from the surface to 50 hPa with denser layers at lower altitudes. The physical options, as well as initial and boundary conditions used in our simulations, follow Zhao et al.[5]

2. Sources of observational data

We evaluate the model simulations using measurements obtained in the GoAmazon (Observations and Modelling of the Green Ocean Amazon) campaign.[14-16] The pollution plumes from Manaus generally follow the easterly trade winds during the simulation period. The Gulfstream 1 (G-1) aircraft was deployed during certain days of the GoAmazon campaign to measure aerosol characteristics downwind (west) of Manaus. As described in the main text, on March 11, 13, and 14, the aircraft flight track passed over Manaus or intersected its pollution plume perpendicular to the prevailing wind direction 4–5 times (Transects P0 to P3/4 in Fig. 1) at increasing distances from Manaus at an altitude of 500–800 m. Based on the average wind speed in the plume, on March 11, the transport times from Transect P0 (right above Manaus) to Transects P1, P2, and P3 are about 1.26 h, 2.34 h, and 3.77 h, respectively. On March 13, the transport times from P0 to P1, P2, P3, and P4 are about 1.15 h, 2.26 h, 3.45 h, and 4.78 h, respectively. On March 14, the transport times from P0 to P1, P2, P3, and P4 are about 1.06 h, 2.08 h, 2.71 h, and 4.28 h, respectively. On March 12, the flight is special in that the plume transects were made in the southernmost parts of the flight tracks (cf. middle parts for other flights) and turn-around flight legs were made to achieve more effective plume transects; the aircraft still periodically passed through in-plume and background air but Transects P0–P3 are not located increasingly farther

downwind as in other flights (see Fig. 1). We use total particle number concentrations measured by a condensation particle counter (CPC, TSI model 3025, cutoff diameter 3 nm) and particle size distributions ranging from 10 nm to 400 nm in diameter characterized by a fast integrated mobility spectrometer (FIMS) at a time resolution of 1 second.[15, 17] We also make use of monoterpene concentrations measured by an Ionicon quadrupole high-sensitivity proton-transfer-reaction mass spectrometer (PTR-MS) onboard G-1.[16] Moreover, we employ measurements of H_2SO_4 by a hydroxyl radical chemical ionization mass spectrometer (CIMS) at the T3 surface site downwind of Manaus (Fig. 1)—the only available H_2SO_4 measurements during the GoAmazon campaign.[18]

Particle number concentration measurements at the T1 surface site in the urban area of Manaus are not available for the simulation period (March 6–15, 2014). Therefore, we employ the measurements during March 6–15 of 2016 made by a scanning mobility particle sizer (SMPS, TSI model 3081) for particles with a diameter of 10–450 nm and conduct additional simulations with exactly the same model configurations during this period to compare with the measurements. Note that the CPC and FIMS aboard the G-1 aircraft and the SMPS at the T1 site are all located behind a dryer. As a result, the sampling relative humidity has remained less than 40% for the whole field campaign, which effectively minimized the potential impact of ambient relative humidity or water supersaturation. For NH_3, no available observations are found within the modeling domain, thus we use NH_3 concentration measurements by a wet-annular denuder at a site in southwest Amazon during the wet season of 2002[19] as a proxy.

3. Supplementary information about model-observation comparison

In the main text, we compared simulated vs. observed particle size distributions (Fig. 3). Since this comparison is limited to particles larger than 10 nm in diameter due to the limitation of FIMS, we further show in Fig. S11 observed particle number concentrations in the diameter range of 3–

10 nm by the G-1 aircraft as well as simulated concentrations during four flights on March 11–14. The observed particle number concentrations between 3 nm and 10 nm are derived from the difference between two CPCs that measure particles larger than 3 nm and 10 nm, respectively.

First, we note that the observed high numbers of particles between 3 and 10 nm in the plumes do indeed confirm that a large fraction of the particle concentrations is probably contributed by NPF. Without NPF, the primarily emitted particles would have grown to larger sizes when they were transported to the locations where they were observed by the G-1 aircraft (see the blue lines in Fig. 3).

Second, we compare the modeled and observed concentrations. It is very challenging for mainstream models to capture the particle distribution below 10 nm because such small particles are very sensitive to even small changes in condensational growth and coagulational scavenging. In our base-case simulation ("inorg+org_R2D-VBS"), the model captures the peak number concentration in the range of 3–10 nm in some of the transects but generally underestimates the peak concentrations in most transects. One likely reason for this bias is that the current model assumes instantaneous equilibrium for gas-particle partitioning of organics instead of considering kinetic partitioning for aerosol growth processes.[20, 21] Another possible reason is that we used a highly condensed 2-bin Volatility Basis Set (VBS) approach to simulate the SOA formation from all precursors other than monoterpenes, including anthropogenic volatile organic compounds (VOC), non-monoterpene biogenic VOC, evaporated primary organic aerosol (POA), and intermediate volatility organic compounds (IVOC). In this simplified scheme, the oxidation products from each type of precursor are assumed to possess the same volatility (C* of 0.01 μg m^{-3} for the oxidation products of evaporated POA and IVOC and 1.0 μg m^{-3} for the oxidation products from anthropogenic VOC and non-monoterpene biogenic VOC), which may bias the size-

dependent growth rates. For example, Zaveri et al.[22] recently showed that assuming the condensable vapors to have low volatility may cause small particles to grow too fast and thus lead to underestimation of the concentration of small particles. In our ongoing work, we are trying to incorporate kinetic organic partitioning in WRF-Chem and simulate the non-monoterpene organic chemistry using an updated 4-bin VBS from Shrivastava et al.[13], which we hope will alleviate the underestimation of particles between 3 nm and 10 nm.

To show that the above bias should not affect the main conclusion of this study regarding the source of particle number, we conduct two sensitivity simulations in which we artificially reduce the particle growth rate either in the entire size range ("slow growth") or only in the size range below 10 nm ("slow growth below 10 nm") to allow more particles to stay in the range of 3–10 nm. Specifically, we assume that only 50% (cf. 100% in the base-case simulation) of the excessive organic vapor (i.e., gas concentration before partitioning − equilibrium gas concentration) will condense to the particle phase in the specified size range in each time step. Fig. S11 shows that both scenarios show higher particle number concentrations between 3 nm and 10 nm compared to the base-case simulation, leading to a much closer agreement with observations, though biases still exist. Fig. S12 further illustrates the fractional contribution of NPF within the modeling domain to particle number concentrations on a 2-km high vertical cross section which extends westward from Manaus to 200 km downwind in the base case and two sensitivity scenarios. The contribution of NPF is quantified using the difference in simulated particle concentrations between one of the three scenarios and a hypothetical scenario without NPF ("nonuc" in Table S2). All three scenarios show similar relative contributions of NPF to particle number concentration in the areas downwind of Manaus, suggesting that the bias in particle growth that leads to the underestimation of 3–10 nm

particles in our current model is not likely to affect our main conclusion that NPF makes the most important contribution to particle number in most of the downwind areas.

We note that the particle number concentrations (> 3 nm) for the "inorg" scenario are sometimes lower than those for the "nonuc" scenario, as shown in Fig. 2. This is probably because the changes in aerosol fields due to inorganic NPF could affect the meteorological fields by interacting with radiation and clouds, which may further perturb particle concentrations at other times and locations. Since the rates of inorganic NPF are small at many times and locations, the accumulated perturbation over time could dominate over the direct particle formation in some circumstances, leading to occasional lower particle number concentrations in the "inorg" scenario than in the "nonuc" scenario. We also note that the simulated particle number at P3 on March 11 is significantly lower than the observed value (Fig. 3a). The main reason is that the simulated centerline of the pollution plume was shifted to some extent relative to the observed location (see Fig. 2a), probably because of uncertainties in the simulated wind direction. As a result, the model underestimates observed particle number concentrations near the location of the observed pollution plume centerline.

As mentioned in the main text, we conduct additional simulations with the same model configurations for March 6–15 in 2016 to compare with measurements at the T1 site. Here we calculate the statistics of major meteorological variables within the modeling domain at the surface level and 500 m height during our main simulation period (March 6–15, 2014) and the above supplementary simulation period, as summarized in Table S3. The temperature and relative humidity are very similar during the two simulation periods. The wind speed is also similar—the mean wind speed is slightly larger in the simulation period of 2014 but the standard deviation is very close in the two periods. The size distribution simulated by the base case ("inorg+org_R2D-

VBS") generally agrees with observations at T1, with a certain level of overestimation in the range of 20–60 nm and underestimation in smaller and larger sizes (Fig. S4). As we discussed above, we expect that the size distribution could be further improved after we incorporate in WRF-Chem kinetic particle growth and improved volatility distribution of organic aerosols in our ongoing work.

4. Relationships between NPF rates and particle number concentrations

The NPF rates shown in Fig. 5 and Fig. S6 are relatively low compared to many field observations[23, 24] because they are averaged during the entire simulation period (March 6–15, 2014) and the data in Fig. 5 are further vertically averaged below 2 km. In contrast, observational studies usually report only the NPF rates during strong NPF events.[23, 24] Fig. S13c shows hourly average NPF rates on a 2-km high vertical cross section that extends westward from Manaus to 200 km downwind during the simulation period. We can see that high hourly average NPF rates larger than 10 cm^{-3} s^{-1} are frequently simulated by the model.

We have also conducted additional analysis on the relationships between NPF rates and particle number concentrations, as shown in Fig. S13. Fig. S13a exhibits the time-averaged NPF rate on the aforementioned vertical cross section and Fig. S13b exhibits the time-averaged particle number concentration increase due to NPF, which is quantified using the difference between the base case ("inorg+org_R2D-VBS") and the scenario without NPF ("nonuc"). Fig. S13c further shows hourly average NPF rate and increased particle number concentration on the cross section. The increased particle number concentrations due to NPF are generally larger in areas with larger NPF rates. There is a statistically significant positive correlation between the two with a correlation coefficient of 0.619 and a p-value < 0.001 (Fig. S13c). However, the relationships are complicated by two factors. First, a large NPF rate is simulated at the surface of the city center but the increase

in particle number concentration is relatively small mainly because of a large coagulational loss caused by direct particle emissions. Second, particles observed in a certain location are not necessarily formed locally but may be transported from upwind areas by the prevailing easterly wind. As a result of the two factors, the increased particle number concentrations due to NPF peak about 30 km downwind of the city center while the NPF rates peak near the city center (Fig. S13a,b). Also, as a result of the two factors, the increase in particle number concentrations has a large variability even for a given NPF rate (Fig. S13c).

5. Details of the sensitivity analysis

We showed in Results and Discussion that primary particle emissions only account for a small fraction of particle number concentration downwind of Manaus. Compared with the particle size distribution used in many previous regional modeling studies,[25-29] the size distribution used in this study results in relatively large total particle number emissions (see Methods and Data). To test potential uncertainties that may lead to even higher particle number emissions and hence a larger contribution to ambient particle number concentrations, we design two sensitivity scenarios by perturbing the total mass emissions ("nonuc_emis*4") and size distribution ("nonuc_emis_finer") on the basis of the scenario without any NPF ("nonuc"). In the "nonuc_emis*4" scenario, we increase the primary particle mass emissions by a factor of 4 while keeping the size distribution unchanged. The particle size distribution used in this study is a superposition of two lognormal distributions with an Aitken mode and an accumulation mode. In the "nonuc_emis_finer" scenario, we reduce the Aitken-mode median diameter of urban sources from 25 nm to 12 nm. The reason is that some emission measurements suggested that the primary particles from certain types of vehicles might have a peak diameter of 10–25 nm,[30-32] smaller than 25 nm assumed for urban emissions in this study. While the effective particle size of emissions at a 10-km grid spacing will

be larger than that of fresh emissions (see Methods and Data) and thus the effective size is unlikely as small as 12 nm, we use this small size as a sensitivity test to examine the potential upper bound of particle number emissions. Particle measurements at the T1 surface site in urban Manaus provide a useful constraint for the estimate of primary particle emissions. Figure S3 shows that both sensitivity scenarios overestimate the particle number concentration at the T1 site by a factor of 2.5–3.2 even without considering NPF. This indicates that the particle number emissions in these two scenarios are likely too high. Even so, Fig. S8 shows that the model still substantially underestimates the aircraft-measured particle number concentration in the Manaus plumes by nearly one order of magnitude. These results indicate that, even with the potential upper bound of the particle number emission estimates, the primary particle emissions are not likely the main sources for the high particle number concentrations in the pollution plumes from Manaus.

Apart from primary emissions, our results also indicate that inorganic NPF pathways make a minor contribution to particle number downwind of Manaus. To investigate the factors that could potentially lead to a larger contribution from inorganic NPF, we conduct two additional sensitivity simulations ("inorg_NH_3*3" and "inorg_amine") based on the scenario of "inorg". Among the precursors for inorganic NPF, the concentrations of NH_3 are subject to a relatively large uncertainty partly due to very limited measurements over the Amazon. The "inorg_NH_3*3" scenario is the same as "inorg" except that the NH_3 concentrations are elevated by a factor of 3. The NPF of H_2SO_4 and amines has also been shown to be an appreciable pathway in certain polluted environments.[33, 34] In the "inorg_amine" scenario, we provide a first-order estimate of the potential contribution of H_2SO_4+amine NPF by incorporating the parameterization developed by Dunne et al.[1] using data from the CLOUD chamber.[35] The amine concentrations have been modeled by several studies with very similar methods; they all derived the amine emission

277 inventory by scaling down ammonia emissions using sector-specific factors.[1, 36, 37] Here we apply
278 the ratio of amine concentration to ammonia concentration simulated by Dunne et al.[1] over our
279 domain to the WRF-Chem/R2D-VBS simulated ammonia concentrations to estimate the amine
280 concentrations, and subsequently use the estimated amine concentrations to calculate the
281 H_2SO_4+amine NPF rate. Note that this scenario merely serves as a rough estimate of the potential
282 contribution of amines rather than a rigorous quantification of the NPF rate. Figure S9 reveals that
283 both the "inorg_NH_3*3" and "inorg_amine" scenarios only slightly amplify simulated particle
284 number concentrations relative to "inorg", which are still far below the concentrations observed
285 by the G-1 aircraft. These results reinforce our findings that inorganic NPF is unlikely the main
286 source of the particle number downwind of Manaus and suggest that our conclusions are robust.
287 The above sensitivity simulations, by testing the potential upper bounds of primary particle
288 emissions and inorganic NPF, increase our confidence that organic-mediated NPF probably acts
289 as the most important source of particle number downwind of Manaus. A sophisticated model
290 representation of organic-mediated NPF is crucially important for reasonably estimating its
291 contribution in polluted environments. Here we conduct two sensitivity simulations to show that
292 previous more simplified model treatments may lead to substantial bias in simulated NPF rates. In
293 the first simulation ("inorg+org_simple"), we assume that the organics contributing to NPF are a
294 fixed fraction of all monoterpene oxidation products, following the common practice of many
295 previous studies.[1, 4, 27, 38-40] The specific fixed fractions we used are from Gordon et al.[4] Figure S10
296 shows that this sensitivity run overestimates the G-1 observed particle number concentrations in
297 Manaus plumes by 1–1.5 orders of magnitude. A major reason, among others, is that this simple
298 treatment fails to capture the strong condensation sink of ULVOC/ELVOC in pollution plumes
299 due to their extremely low volatilities. In another sensitivity scenario ("inorg+org_R2D-

VBS_uniauto"), we apply an older version of the Radical 2D-VBS used in Zhao et al.[5] The difference between the two versions is that the older version used a uniform autoxidation rate for all RO_2 of the same generation. Figure S10 reveals that this scenario significantly underestimates peak particle number concentrations in Manaus plumes by over one order of magnitude, indicating that the prompt ELVOC formation through rapid autoxidation is critically important to effectively compete with the condensation loss in urban plumes and to produce a considerable number of new particles. While a uniform autoxidation rate can reasonably simulate the particle formation in pristine conditions,[5] an appropriate representation of diversity in ELVOC formation rate is necessary for polluted regions with a large condensation loss. The inorganic species involved in NPF comprise a relatively small set; the organics are numerous, spanning a wide range in volatility and also reactivity. The Radical 2D-VBS represents a substantial simplification over a full chemical description. Our results reveal that further reducing the complexity much beyond this point introduces measurable errors into real-world model outputs.

6. Discussion of the potential impact of other precursors and processes

In our current model, we use monoterpenes as the main precursors to drive organic-mediated NPF, because monoterpenes have been well recognized to be an important contributor to NPF since the oxidation of monoterpene produces a significant amount of ULVOC and ELVOC. It is noted, however, that other organic precursors may also have (enhancement or suppression) effects on NPF.

In contrast to monoterpenes, isoprene has been much less frequently observed to trigger NPF[41] but has been frequently shown to suppress NPF events.[42-44] Regarding NPF triggered by isoprene, Inomata et al.[41] showed that the ozonolysis of isoprene produces stabilized Criegee intermediates and subsequently oligomeric hydroperoxides, which contribute to NPF under dry conditions.

However, the isoprene concentrations used in that experiment (~2 ppm) are approximately 3 orders of magnitude higher than the isoprene concentrations observed in our region of interest (0.43–2.37 ppb).[16] Besides, Inomata et al.[41] showed that the NPF triggered by isoprene oxidation products is substantially suppressed when relative humidity is larger than 68%. The relative humidity within our domain is as high as 89.6±11.6% at the surface level and 87.5±9.2 at 500 m height during our simulation period (Table S3), which is high enough to largely suppress isoprene-induced NPF. Compared with the limited evidence for NPF driven by isoprene, more studies have revealed that isoprene suppresses the NPF triggered by monoterpene oxidation products,[42-44] probably because isoprene reduces the yield of highly-oxygenated dimers with about 20 carbon atoms that drive NPF while increasing the production of "heterodimers" with about 15 carbon atoms (isoprene-monoterpene cross reaction products).[44] For these reasons, we conclude that isoprene is not likely to play a dominant role in driving NPF over the Amazon, but future research is still needed to quantify the effects of isoprene on NPF rates. In addition, some studies have reported that sesquiterpenes might make a noticeable contribution to NPF despite their much smaller concentrations than monoterpenes,[45] but it is still difficult to accurately quantify their contribution based on currently limited results. More recently, it was found that the oxidation of anthropogenic organic precursors may also produce oxidation products with sufficiently low volatility to trigger NPF in polluted environments.[46, 47] For example, Wang et al.[47] showed that the oxidation products of toluene have a similar volatility distribution to that of α-pinene oxidation products, while the oxidation products of naphthalene are even less volatile than those from toluene or α-pinene. Their importance for NPF relative to biogenic precursors, however, remain largely unknown because 1) the yields of ULVOC/ELVOC from anthropogenic precursors remain unclear; and 2) a large fraction of the ULVOC/ELVOC from these precursors is produced by slower multi-generational

346 oxidation reactions (relative to the rapid autoxidation in the case of monoterpenes), while a rapid
347 formation of ULVOC/ELVOC is important to effectively compete with the strong condensation
348 loss in polluted areas. The net organic NPF rate in the real world is likely a combined effect of all
349 aforementioned precursors, with some precursors accelerating while others slowing down the NPF
350 rates given by our current model.

351 In addition to the NPF rate, the growth and removal of particles also affect the ambient particle
352 number. After ELVOC, most typically multifunctional hydroperoxides formed via autoxidation,
353 partition to the particle phase, they may undergo further particle-phase reactions, including
354 accretion reactions leading to oligomers and decomposition leading to shorter-chain compounds.[48,
355 49] Pospisilova et al.[48] suggested that the particle-phase reactions in α-pinene ozonolysis
356 experiments are likely dominated by the decomposition of reactive oxygen species, including
357 hydroperoxides. The lifetimes of these species against particle-phase reactions could span a large
358 range,[49] but are mostly about 30 to 150 min for α-pinene ozonolysis products.[48] The particle-phase
359 reactions result in continuous concentration and composition changes of SOA. The effect on NPF
360 remains unclear. The decomposition reaction might accelerate the evaporation of newly formed
361 particles and reduce the effective NPF rate; however, it is more likely that decomposition could
362 slow the growth rate of newly formed particles but not lead to complete evaporation. Even that is
363 uncertain. Decomposition products will not necessarily evaporate, and our results show that the
364 overall environment in the pollution plume is dominated by SOA formation and particle growth.
365 Thus, the particle-phase reactions are not likely to greatly change the NPF rate. Nevertheless,
366 future studies are needed to quantify the effect of particle-phase reactions on SOA and NPF in our
367 model. Furthermore, while our current model simulates the particle growth by condensation of
368 organics using an equilibrium partitioning method, recent studies showed that the growth and

369 evaporation kinetics can affect the size distribution evolution[20, 21] and thus needs to be considered
370 in future studies to better simulate the particle growth and size distribution in the pollution plumes.
371 For example, the diameter of the simulated peak number concentration grows slower than observed
372 as show in Fig. 3. The underestimate of particles in the range of 3–10 nm may also be partly
373 attributed to this issue (see more in Section 3 of SI). Finally, the chemical loss of organic particles
374 via photolysis[50] also needs to be accounted for to properly simulate the lifecycle and budget of
375 particles.

376 ## 7. Discussion of the role of H_2SO_4 monomer and dimer

377 H_2SO_4 dimer is an important intermediate for many types of NPFs involving H_2SO_4. For acid-
378 base nucleation, such as the nucleation of H_2SO_4 with amine or NH_3, H_2SO_4 dimer plays a key
379 role in the nucleation process.[35, 51] For the nucleation of H_2SO_4 with organics, the main NPF
380 pathway in our region of interest, the situation is more complex. According to the mass defect
381 diagrams for negatively charged clusters during NPF experiments involving H_2SO_4 and organics
382 at the CLOUD chamber (Fig. 2a of Riccobono et al.[2] and Fig. 1c of Schobesberger et al.[52]), there
383 are many clusters of H_2SO_4 dimer with organics but there are even more clusters of H_2SO_4
384 monomer with organics. This indicates that the H_2SO_4 dimer is likely to play a certain but not the
385 most important role in the nucleation of H_2SO_4 with organics.

Figures and Tables

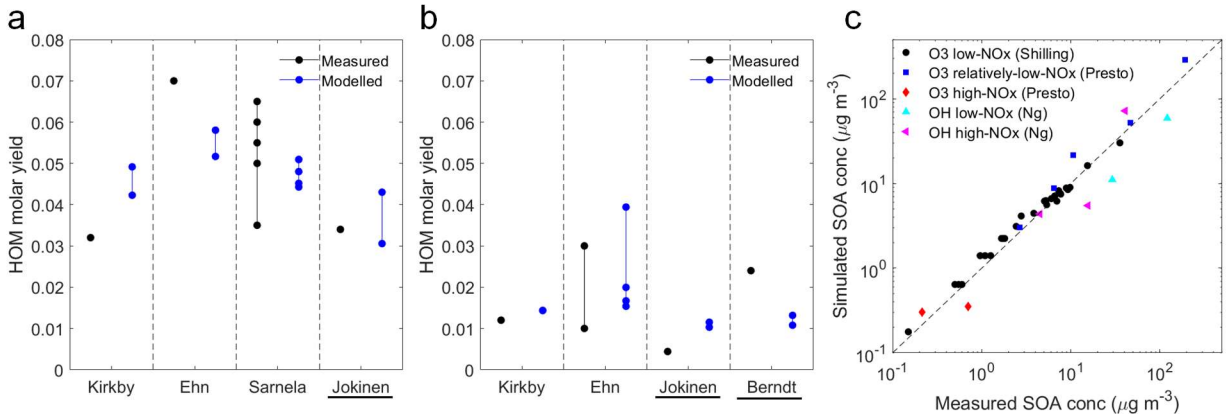

Figure S1. Comparison of Radical 2D-VBS simulated HOM yields and SOA concentrations with smog-chamber and flow-tube experiments: (a) HOM molar yields from α-pinene + O_3, (b) HOM molar yields from α-pinene + OH, and (c) SOA concentrations. The simulation results are obtained with the final Radical 2D-VBS parameters used in our 3-D simulations. The measurements of α-pinene + O_3 HOM molar yields are from Kirkby et al.[3], Ehn et al.[53], Sarnela et al.[54], and Jokinen et al.[6]; the measurements of α-pinene + OH HOM molar yields are from Kirkby et al.[3], Ehn et al.[53], Jokinen et al.[6], and Berndt et al.[55]; and the measurements of SOA concentrations are from Shilling et al.[56], Presto and Donahue[57], and Ng et al.[58]. In (a) and (b), each dot represents the measured HOM yield for an experiment or the simulated HOM yield for a model run (see a list of all model runs in Table S2 and S3 of Zhao et al.[5]). For some studies (Kirkby, Ehn, and Jokinen in (a); Kirkby, Jokinen, and Berndt in (b)), we only show one dot for measurements because the corresponding literature only reports the mean HOM yield for all experiments. The studies highlighted with an underline are flow-tube experiments.

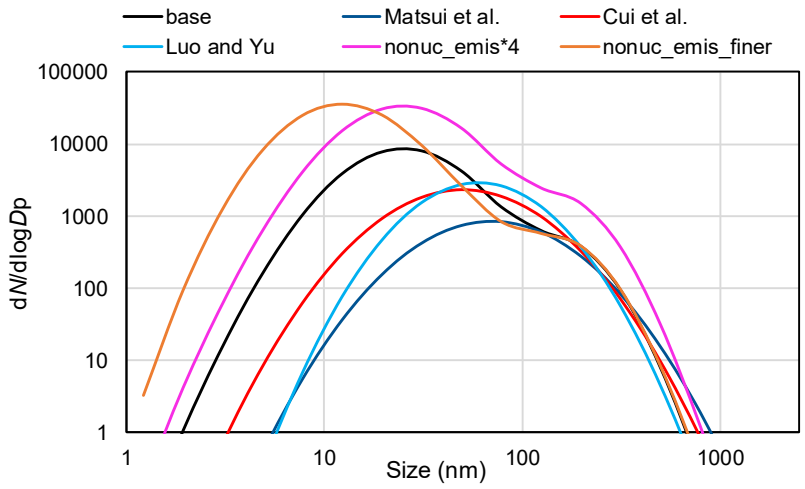

Figure S2. Number density per pg (10^{-12} g) of primary particle emissions, according to the size distribution used in the base case of this study ("base" in the figure), a number of previous regional modeling studies ("Matsui et al.", "Cui et al.", and "Luo and Yu"), and two sensitivity cases in this study ("nonuc_emis*4" and "nonuc_emis_finer"). For the "nonuc_emis*4" case, the figure shows the number density per 4 pg of primary particle emissions. The size distribution of "Matsui et al." has been used in Matsui et al.[25]; "Cui et al." has been used in Cui et al.[26] and Lupascu et

al.[27]; "Luo and Yu" has been used in Luo and Yu[28], Yu et al.[59], Chen et al.[60], and Chen et al.[29]. Note that in the base case and the two sensitivity cases ("nonuc_emis*4" and "nonuc_emis_finer"), we assume the mass fraction of Aitken-mode particles to be 30% (cf. the baseline estimate of 10% in Elleman and Covert[61]) for non-industrial urban sources in Manaus, which represents an urban environment with a relatively high contribution from transportation emissions.

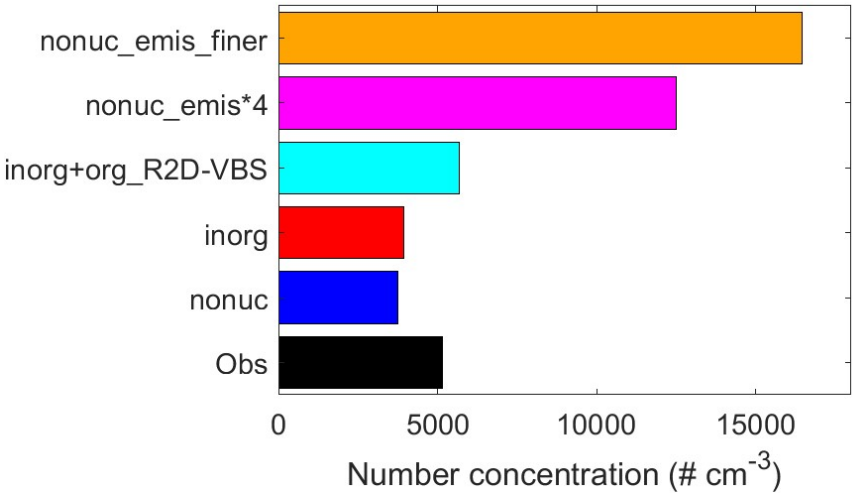

Figure S3. Comparison of simulated particle number concentrations (> 10 nm) averaged during March 6–15, 2016 with surface observations at the T1 site. The number concentrations are normalized to STP. The definitions of the model scenarios are summarized in Table S2.

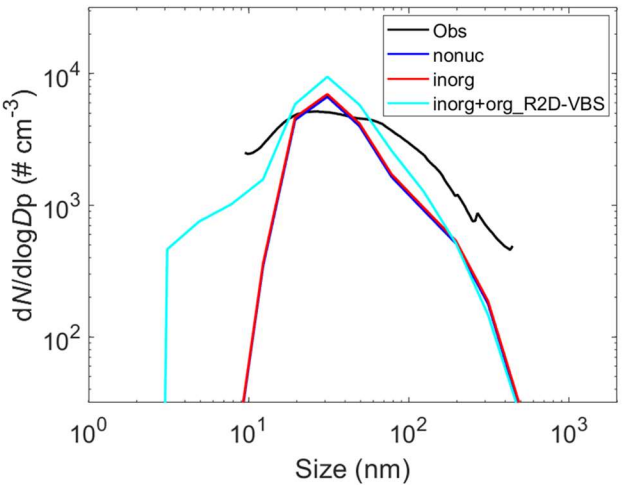

Figure S4. Comparison of simulated particle number size distribution with surface observations at the T1 site during March 6–15, 2016. The particle size distributions are normalized to STP. The definitions of the model scenarios are provided in the main text and Table S2.

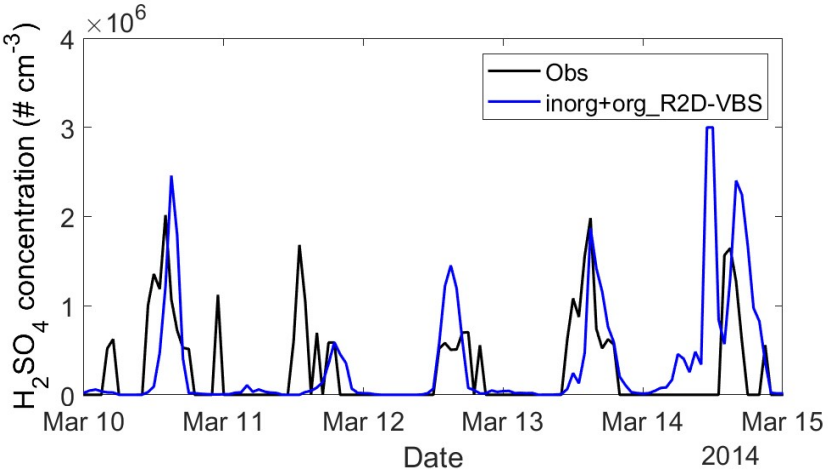

Figure S5. Comparison of simulated H_2SO_4 concentrations simulated by the base case ("inorg+org_R2D-VBS") with surface observations at the T3 site. The concentrations are normalized to STP.

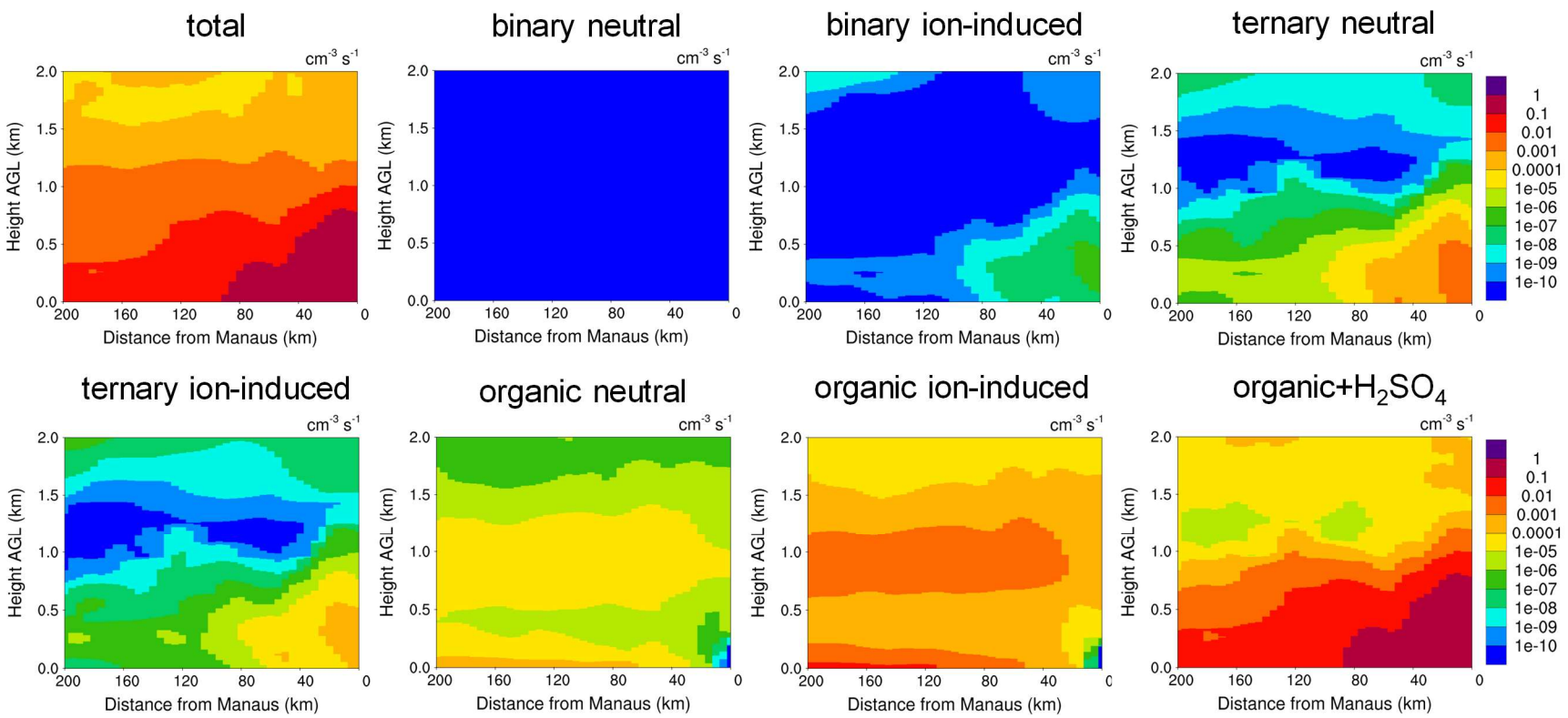

Figure S6. NPF rates from seven pathways and the total NPF rate at a diameter of 1.7 nm ($J_{1.7}$) on the 2-km high vertical cross section defined in Fig. 4, simulated by the base case ("inorg+org_R2D-VBS"). The results are averaged during the simulation period of this study.

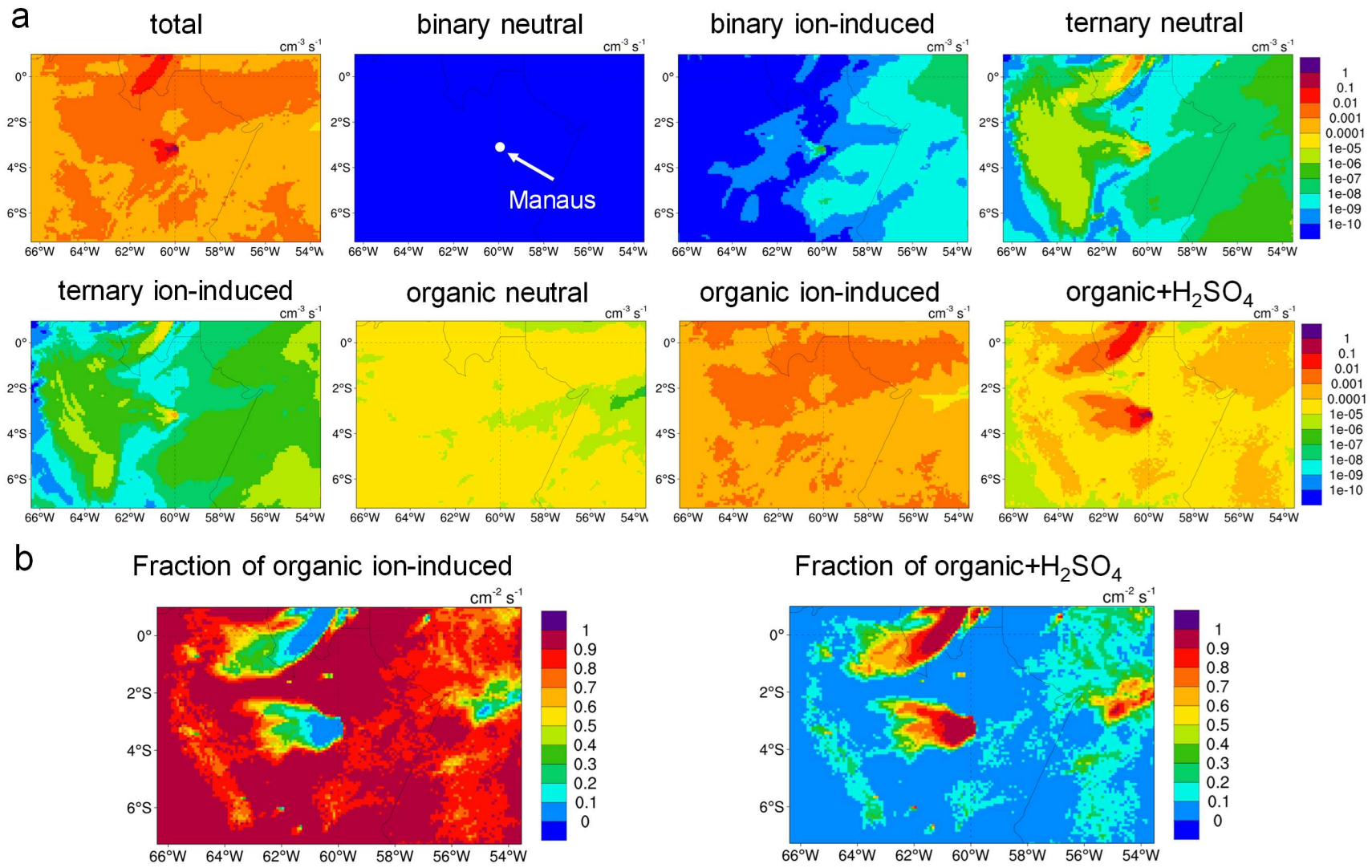

Figure S7. Spatial distribution of the contribution of different NPF pathways. (a) NPF rates from seven pathways and the total NPF rate at a diameter of 1.7 nm ($J_{1.7}$) vertically averaged below 2 km, simulated by the base case ("inorg+org_R2D-VBS"). (b) The relative contribution of the pure-organic ion-induced and organic+H_2SO_4 pathways to total NPF rate. The results are averaged during the simulation period of this study.

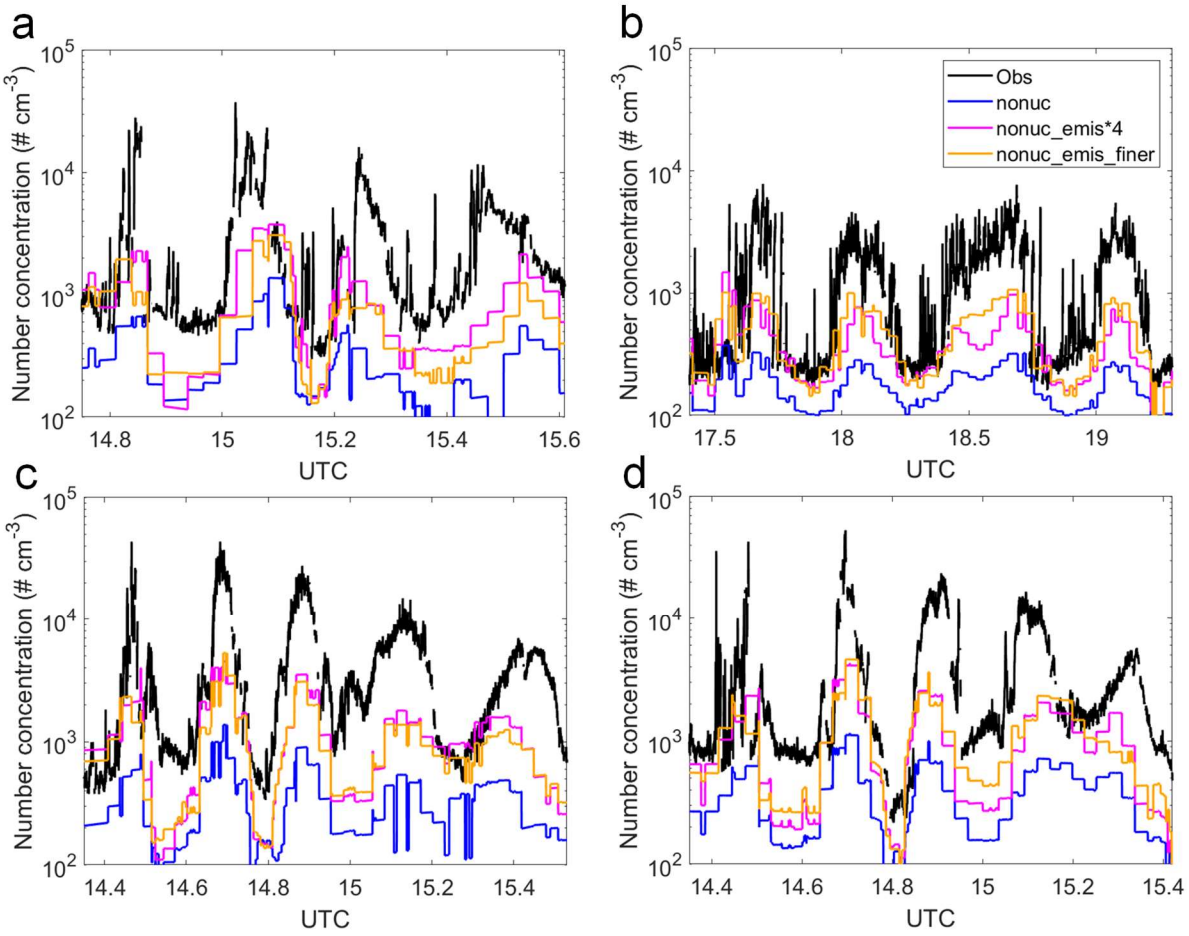

Figure S8. The same as Fig. 2 but for the "nonuc" scenario and two sensitivity scenarios perturbing the emission inventory. The definitions of the model scenarios are summarized in Table S2.

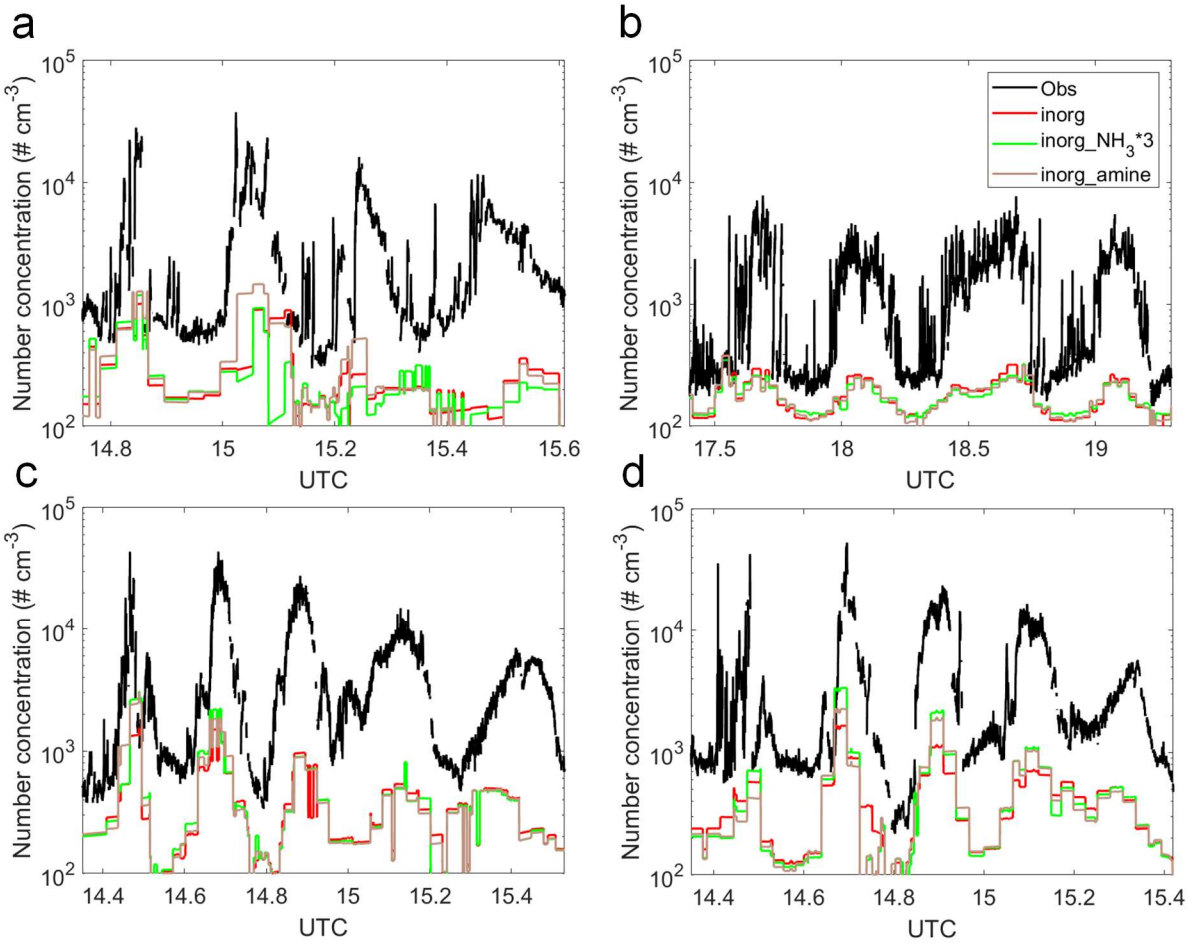

Figure S9. The same as Fig. 2 but for the "inorg" scenario, a sensitivity scenario perturbing NH_3 concentration, and a sensitivity scenario adding an NPF pathway involving H_2SO_4 and amines. The definitions of the model scenarios are summarized in Table S2.

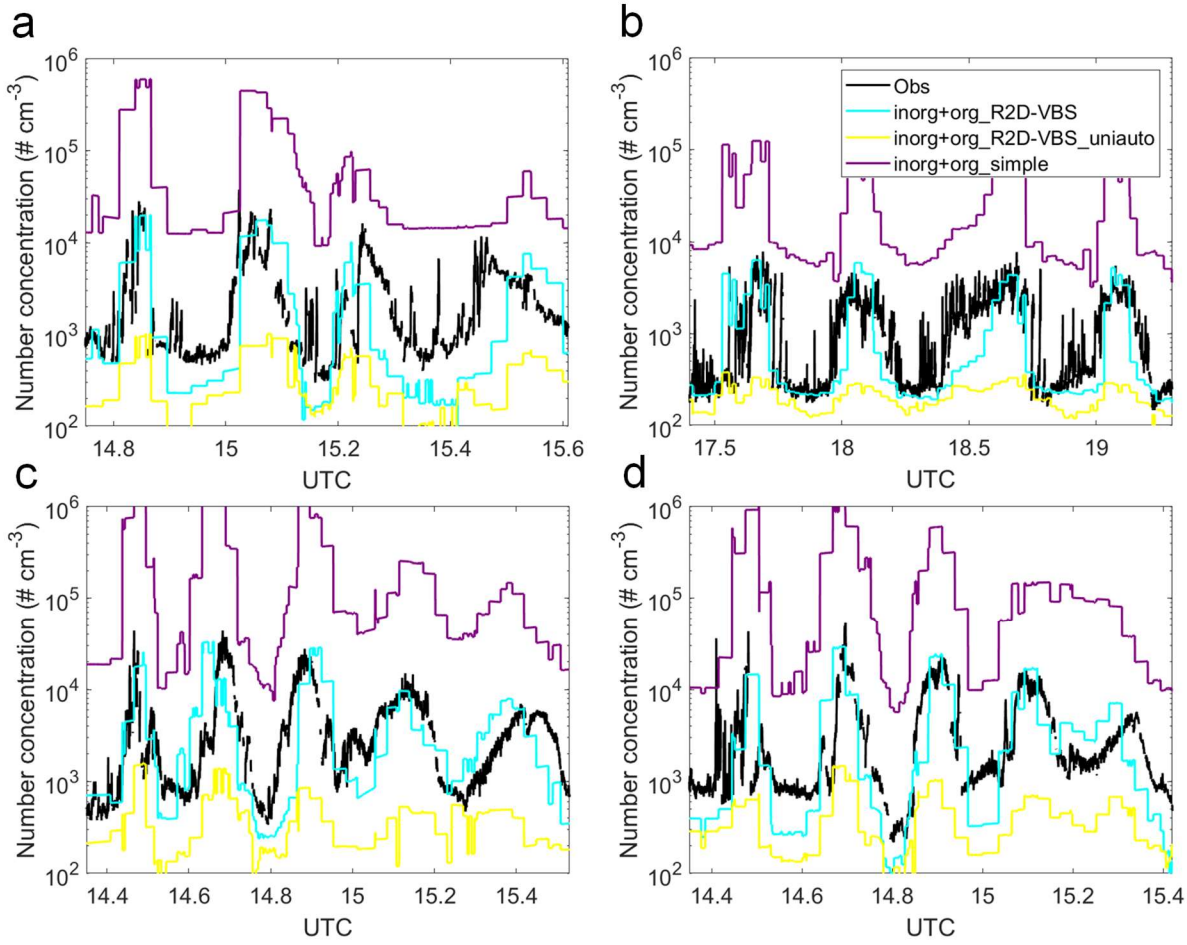

Figure S10. The same as Fig. 2 but for the base case (i.e., inorg+org_R2D-VBS) and two sensitivity scenarios with different treatments of the formation chemistry of the organics that drive NPF. The definitions of the model scenarios are summarized in Table S2.

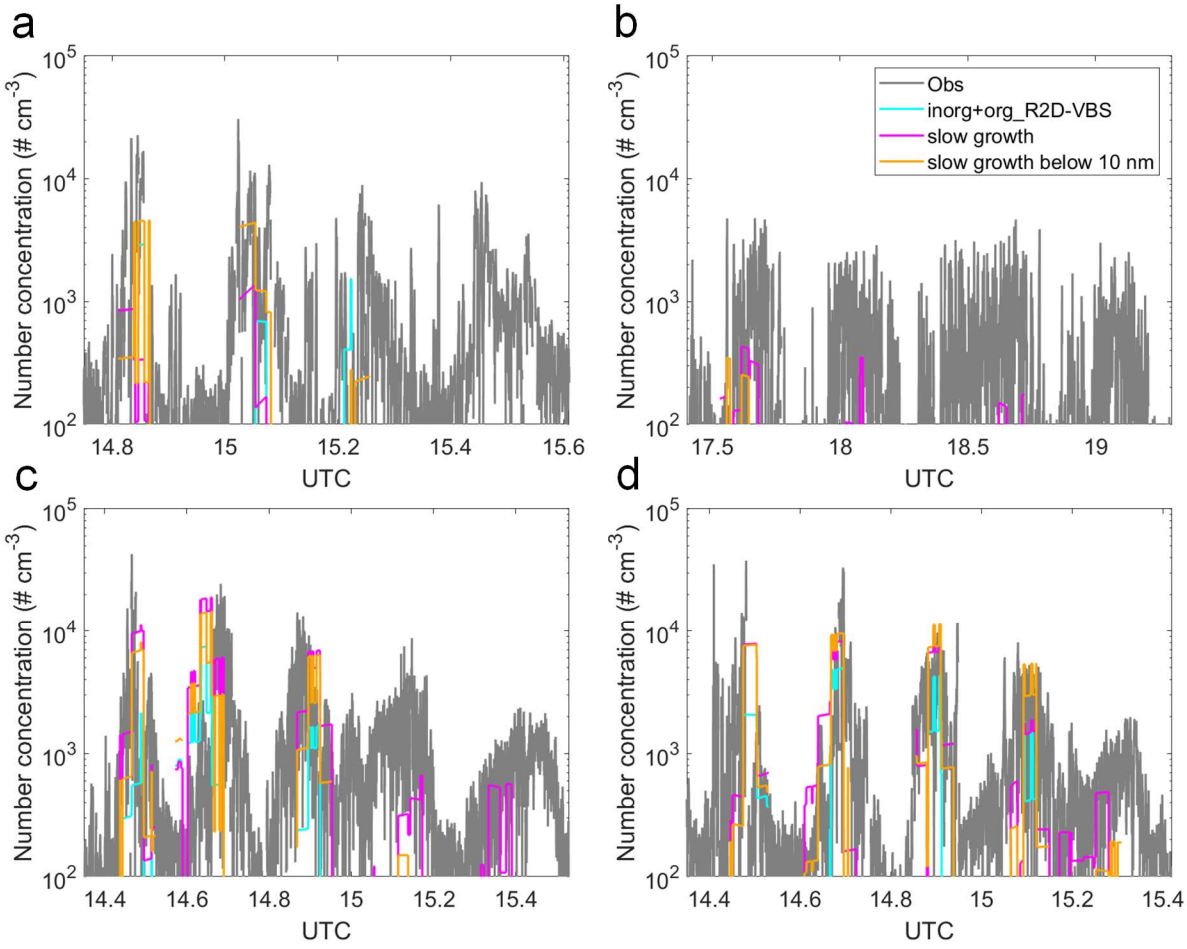

Figure S11. Comparison of simulated particle number concentration in the range of 3–10 nm with G-1 aircraft measurements. (a) March 11, (b) March 12, (c) March 13, and (d) March 14, 2014. The particle number concentrations are normalized to STP. The definitions of the model scenarios are provided in the main text and Table S2.

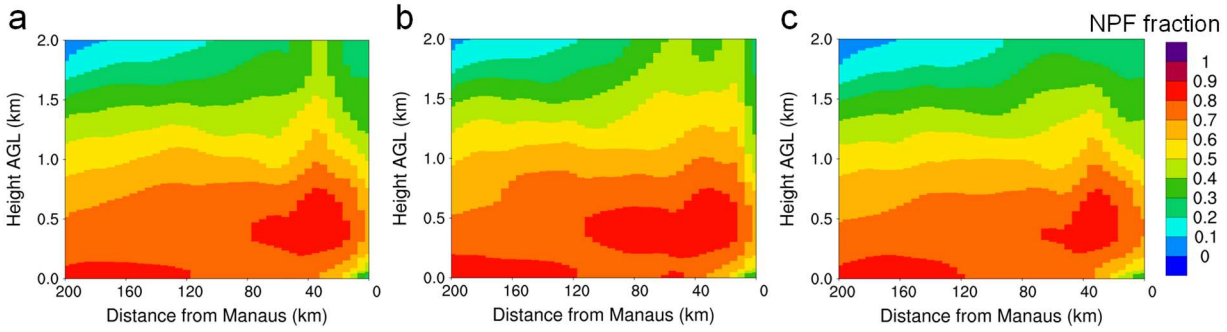

Figure S12. The fractional contribution of NPF within the modeling domain to particle number concentrations on a 2-km high vertical cross section which extends westward from Manaus to 200 km downwind, simulated by (a) the base case, i.e., "inorg+org_R2D-VBS", (b) the scenario of "slow growth", and (c) the scenario of "slow growth below 10 nm". The position of the cross section is marked with a white arrow in Fig. 4d. The results are averaged during the simulation period of this study (March 6–15, 2014).

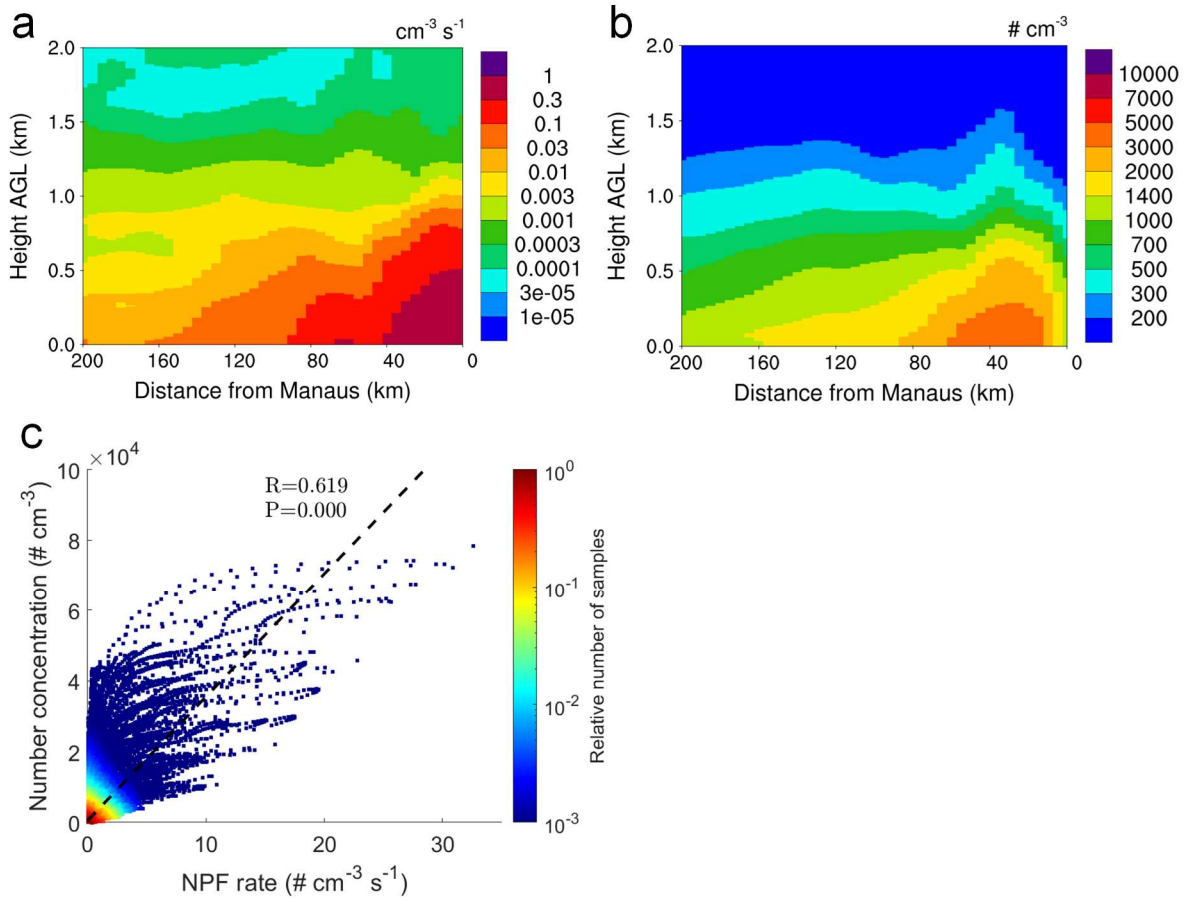

Figure S13. Relationships between NPF rate and increased particle number concentration due to NPF. (a) NPF rate on a 2-km high vertical cross section which extends westward from Manaus to 200 km downwind. (b) Increased particle number concentration due to NPF on the cross section, which is quantified using the difference between the base case ("inorg+org_R2D-VBS") and the scenario without NPF ("nonuc"). The data in (a) and (b) are averaged during the simulation period of this study (March 6–15, 2014). (c) Scattering plot of hourly average NPF rate vs. increased particle number concentration due to NPF on the cross section during the simulation period. The position of the cross section is marked with a white arrow in Fig. 4d.

Table S1. Parameters in the NPF model.

Parameter	Value	Parameter	Value
$p_{b,n}$	3.95451	$p_{b,i}$	3.373738
$u_{b,n}$	9.702973	$u_{b,i}$	−11.48166
$v_{b,n}$	12.62259	$v_{b,i}$	25.49469
$w_{b,n}$	−0.007066146	$w_{b,i}$	0.1810722
$p_{t,n}$	2.891024	$p_{t,i}$	3.138719
$u_{t,n}$	182.4495	$u_{t,i}$	−23.8002
$v_{t,n}$	1.203451	$v_{t,i}$	37.03029
$w_{t,n}$	−4.188065	$w_{t,i}$	0.227413
$p_{A,n}$	8.003471	$p_{A,i}$	3.071246
a_n	1.5703478×10^{-6}	a_i	0.0048314
k_{SA-Org}	3.27×10^{-21}	a_1	0.0400097
a_2	1.84826	a_3	0.00136641
a_4	1.56588	a_5	0.186303
$k_{SA-Amine-1}$	2.08×10^{-25}	$k_{SA-Amine-2}$	1.93×10^{-28}

Note: Full numerical precision is needed. The units of $[ULVOC_{O:C>0.4}]$ are 10^7 cm^{-3}. $[H_2SO_4]$ has units 10^6 cm^{-3} in J_{SA} and $J_{SA,NH3}$, and cm^{-3} in J_{SA-org} and $J_{SA-Amine}$. $[NH_3]$ has units 10^6 cm^{-3} and $[DMA]$ has units cm^{-3}. The ion and $[ELVOC_{O:C>0.4}]$ concentrations have units cm^{-3}.

Table S2. Summary of model scenarios developed in this study.

Scenario	Description
Main scenarios	
nonuc	A simulation without NPF.
inorg	A simulation with only inorganic NPF included.
inorg+org_R2D-VBS	A simulation with both inorganic and organic NPF included, and the organics that nucleate are simulated employing the updated Radical 2D-VBS that uses two types of autoxidizable RO_2 with faster and slower autoxidation rates. This is considered as the base-case scenario and is used in most analyses of the present study.
Sensitivity scenarios	
nonuc_emis*4	Based on "nonuc", this scenario increases primary particle emissions by a factor of 4.
nonuc_emis_finer	Based on "nonuc", this scenario reduces the Aitken-mode median diameter of primary particle emissions from urban sources from 25 nm to 12 nm.
inorg_NH_3*3	The same as "inorg" except that the NH_3 concentrations across the domain are increased by a factor of 3.
inorg_amine	The same as "inorg" except that an NPF pathway involving H_2SO_4 and amines is incorporated.

inorg+org_simple	The same as "inorg+org_R2D-VBS" except that the organics that nucleate are assumed to be a fixed fraction of all monoterpene oxidation products.
inorg+org_R2D-VBS_uniauto	The same as "inorg+org_R2D-VBS" except that a uniform autoxidation rate is used for all RO_2 of the same generation.

476

477 **Table S3.** Statistics (mean ± standard deviation) of major meteorological variables within the
478 modeling domain during the main simulation period in March 2014 and supplementary simulation
479 period in March 2016.

	March 6–15, 2014		March 6–15, 2016	
	surface	500 m	surface	500 m
Temperature (K)	298.13±2.31	296.41±1.56	298.83±2.13	297.03±1.39
Relative humidity (%)	89.55±11.62	87.49±9.16	91.35±10.64	89.63±8.04
East-west wind (m s^{-1})	−1.11±1.13	−3.65±2.70	−0.75±1.09	−2.68±2.61
South-north wind (m s^{-1})	−0.35±1.27	−2.07±2.91	−0.18±1.23	−1.36±2.77

480

REFERENCES

1. Dunne, E. M.; Gordon, H.; Kurten, A.; Almeida, J.; Duplissy, J.; Williamson, C.; Ortega, I. K.; Pringle, K. J.; Adamov, A.; Baltensperger, U.; Barmet, P.; Benduhn, F.; Bianchi, F.; Breitenlechner, M.; Clarke, A.; Curtius, J.; Dommen, J.; Donahue, N. M.; Ehrhart, S.; Flagan, R. C.; Franchin, A.; Guida, R.; Hakala, J.; Hansel, A.; Heinritzi, M.; Jokinen, T.; Kangasluoma, J.; Kirkby, J.; Kulmala, M.; Kupc, A.; Lawler, M. J.; Lehtipalo, K.; Makhmutov, V.; Mann, G.; Mathot, S.; Merikanto, J.; Miettinen, P.; Nenes, A.; Onnela, A.; Rap, A.; Reddington, C. L. S.; Riccobono, F.; Richards, N. A. D.; Rissanen, M. P.; Rondo, L.; Sarnela, N.; Schobesberger, S.; Sengupta, K.; Simon, M.; Sipilaa, M.; Smith, J. N.; Stozkhov, Y.; Tome, A.; Trostl, J.; Wagner, P. E.; Wimmer, D.; Winkler, P. M.; Worsnop, D. R.; Carslaw, K. S., Global atmospheric particle formation from CERN CLOUD measurements. *Science* **2016,** *354*, (6316), 1119-1124.
2. Riccobono, F.; Schobesberger, S.; Scott, C. E.; Dommen, J.; Ortega, I. K.; Rondo, L.; Almeida, J.; Amorim, A.; Bianchi, F.; Breitenlechner, M.; David, A.; Downard, A.; Dunne, E. M.; Duplissy, J.; Ehrhart, S.; Flagan, R. C.; Franchin, A.; Hansel, A.; Junninen, H.; Kajos, M.; Keskinen, H.; Kupc, A.; Kurten, A.; Kvashin, A. N.; Laaksonen, A.; Lehtipalo, K.; Makhmutov, V.; Mathot, S.; Nieminen, T.; Onnela, A.; Petaja, T.; Praplan, A. P.; Santos, F. D.; Schallhart, S.; Seinfeld, J. H.; Sipila, M.; Spracklen, D. V.; Stozhkov, Y.; Stratmann, F.; Tome, A.; Tsagkogeorgas, G.; Vaattovaara, P.; Viisanen, Y.; Vrtala, A.; Wagner, P. E.; Weingartner, E.; Wex, H.; Wimmer, D.; Carslaw, K. S.; Curtius, J.; Donahue, N. M.; Kirkby, J.; Kulmala, M.; Worsnop, D. R.; Baltensperger, U., Oxidation products of biogenic emissions contribute to nucleation of atmospheric particles. *Science* **2014,** *344*, (6185), 717-721.
3. Kirkby, J.; Duplissy, J.; Sengupta, K.; Frege, C.; Gordon, H.; Williamson, C.; Heinritzi, M.; Simon, M.; Yan, C.; Almeida, J.; Trostl, J.; Nieminen, T.; Ortega, I. K.; Wagner, R.; Adamov, A.; Amorim, A.; Bernhammer, A. K.; Bianchi, F.; Breitenlechner, M.; Brilke, S.; Chen, X. M.; Craven, J.; Dias, A.; Ehrhart, S.; Flagan, R. C.; Franchin, A.; Fuchs, C.; Guida, R.; Hakala, J.; Hoyle, C. R.; Jokinen, T.; Junninen, H.; Kangasluoma, J.; Kim, J.; Krapf, M.; Kurten, A.; Laaksonen, A.; Lehtipalo, K.; Makhmutov, V.; Mathot, S.; Molteni, U.; Onnela, A.; Perakyla, O.; Piel, F.; Petaja, T.; Praplan, A. P.; Pringle, K.; Rap, A.; Richards, N. A. D.; Riipinen, I.; Rissanen, M. P.; Rondo, L.; Sarnela, N.; Schobesberger, S.; Scott, C. E.; Seinfeld, J. H.; Sipila, M.; Steiner, G.; Stozhkov, Y.; Stratmann, F.; Tome, A.; Virtanen, A.; Vogel, A. L.; Wagner, A. C.; Wagner, P. E.; Weingartner, E.; Wimmer, D.; Winkler, P. M.; Ye, P. L.; Zhang, X.; Hansel, A.; Dommen, J.; Donahue, N. M.; Worsnop, D. R.; Baltensperger, U.; Kulmala, M.; Carslaw, K. S.; Curtius, J., Ion-induced nucleation of pure biogenic particles. *Nature* **2016,** *533*, (7604), 521-526.
4. Gordon, H.; Kirkby, J.; Baltensperger, U.; Bianchi, F.; Breitenlechner, M.; Curtius, J.; Dias, A.; Dommen, J.; Donahue, N. M.; Dunne, E. M.; Duplissy, J.; Ehrhart, S.; Flagan, R. C.; Frege, C.; Fuchs, C.; Hansel, A.; Hoyle, C. R.; Kulmala, M.; Kurten, A.; Lehtipalo, K.; Makhmutov, V.; Molteni, U.; Rissanen, M. P.; Stozkhov, Y.; Trostl, J.; Tsagkogeorgas, G.; Wagner, R.; Williamson, C.; Wimmer, D.; Winkler, P. M.; Yan, C.; Carslaw, K. S., Causes and importance of new particle formation in the present-day and preindustrial atmospheres. *J Geophys Res-Atmos* **2017,** *122*, (16), 8739-8760.
5. Zhao, B.; Shrivastava, M.; Donahue, N. M.; Gordon, H.; Schervish, M.; Shilling, J. E.; Zaveri, R. A.; Wang, J.; Andreae, M. O.; Zhao, C.; Gaudet, B.; Liu, Y.; Fan, J. W.; Fast, J. D., High concentration of ultrafine particles in the Amazon free troposphere produced by organic new particle formation. *P Natl Acad Sci USA* **2020,** *117*, (41), 25344-25351.

6. Jokinen, T.; Berndt, T.; Makkonen, R.; Kerminen, V. M.; Junninen, H.; Paasonen, P.; Stratmann, F.; Herrmann, H.; Guenther, A. B.; Worsnop, D. R.; Kulmala, M.; Ehn, M.; Sipila, M., Production of extremely low volatile organic compounds from biogenic emissions: Measured yields and atmospheric implications. *P Natl Acad Sci USA* **2015,** *112*, (23), 7123-7128.
7. Li, X. X.; Chee, S.; Hao, J. M.; Abbatt, J. P. D.; Jiang, J. K.; Smith, J. N., Relative humidity effect on the formation of highly oxidized molecules and new particles during monoterpene oxidation. *Atmos Chem Phys* **2019,** *19*, (3), 1555-1570.
8. Zaveri, R. A.; Easter, R. C.; Fast, J. D.; Peters, L. K., Model for simulating aerosol interactions and chemistry (MOSAIC). *J Geophys Res-Atmos* **2008,** *113*, (D13), D13204.
9. Hanson, D. R., Mass accommodation of H2SO4 and CH3SO3H on water-sulfuric acid solutions from 6% to 97% RH. *J Phys Chem A* **2005,** *109*, (31), 6919-6927.
10. Fahey, K. M.; Pandis, S. N., Optimizing model performance: variable size resolution in cloud chemistry modeling. *Atmos Environ* **2001,** *35*, (26), 4471-4478.
11. Guenther, A. B.; Jiang, X.; Heald, C. L.; Sakulyanontvittaya, T.; Duhl, T.; Emmons, L. K.; Wang, X., The Model of Emissions of Gases and Aerosols from Nature version 2.1 (MEGAN2.1): an extended and updated framework for modeling biogenic emissions. *Geosci Model Dev* **2012,** *5*, (6), 1471-1492.
12. Zhao, C.; Huang, M. Y.; Fast, J. D.; Berg, L. K.; Qian, Y.; Guenther, A.; Gu, D. S.; Shrivastava, M.; Liu, Y.; Walters, S.; Pfister, G.; Jin, J. M.; Shilling, J. E.; Warneke, C., Sensitivity of biogenic volatile organic compounds to land surface parameterizations and vegetation distributions in California. *Geosci Model Dev* **2016,** *9*, (5), 1959-1976.
13. Shrivastava, M.; Andreae, M. O.; Artaxo, P.; Barbosa, H. M. J.; Berg, L. K.; Brito, J.; Ching, J.; Easter, R. C.; Fan, J. W.; Fast, J. D.; Feng, Z.; Fuentes, J. D.; Glasius, M.; Goldstein, A. H.; Alves, E. G.; Gomes, H.; Gu, D.; Guenther, A.; Jathar, S. H.; Kim, S.; Liu, Y.; Lou, S. J.; Martin, S. T.; McNeill, V. F.; Medeiros, A.; de Sa, S. S.; Shilling, J. E.; Springston, S. R.; Souza, R. A. F.; Thornton, J. A.; Isaacman-VanWertz, G.; Yee, L. D.; Ynoue, R.; Zaveri, R. A.; Zelenyuk, A.; Zhao, C., Urban pollution greatly enhances formation of natural aerosols over the Amazon rainforest. *Nat Commun* **2019,** *10*, 1046.
14. Martin, S. T.; Artaxo, P.; Machado, L.; Manzi, A. O.; Souza, R. A. F.; Schumacher, C.; Wang, J.; Biscaro, T.; Brito, J.; Calheiros, A.; Jardine, K.; Medeiros, A.; Portela, B.; de Sa, S. S.; Adachi, K.; Aiken, A. C.; Albrecht, R.; Alexander, L.; Andreae, M. O.; Barbosa, M. J.; Buseck, P.; Chand, D.; Comstock, J. M.; Day, D. A.; Dubey, M.; Fan, J.; Fast, J.; Fisch, G.; Fortner, E.; Giangrande, S.; Gilles, M.; Goldststein, A. H.; Guenther, A.; Hubbe, J.; Jensen, M.; Jimenez, J. L.; Keutsch, F. N.; Kim, S.; Kuang, C.; Laskskin, A.; McKinney, K.; Mei, F.; Miller, M.; Nascimento, R.; Pauliquevis, T.; Pekour, M.; Peres, J.; Petaja, T.; Pohlker, C.; Poschl, U.; Rizzo, L.; Schmid, B.; Shilling, J. E.; Dias, M. A. S.; Smith, J. N.; Tomlmlinson, J. M.; Tota, J.; Wendisch, M., The Green Ocean Amazon experiment (GoAmazon2014/5) observes pollution affecting gases, aerosols, clouds, and rainfall over the rain forest. *B Am Meteorol Soc* **2017,** *98*, (5), 981-997.
15. Wang, J.; Krejci, R.; Giangrandel, S.; Kuang, C.; Barbosa, H. M. J.; Brito, J.; Carbone, S.; Chi, X. G.; Comstock, J.; Ditas, F.; Lavric, J.; Manninen, H. E.; Mei, F.; Moran-Zuloaga, D.; Pohlker, C.; Pohlker, M. L.; Saturno, J.; Schmid, B.; Souza, R. A. F.; Springston, S. R.; Tomlinson, J. M.; Toto, T.; Walter, D.; Wimmer, D.; Smith, J. N.; Kulmala, M.; Machado, L. A. T.; Artaxo, P.; Andreae, M. O.; Petaja, T.; Martin, S. T., Amazon boundary layer aerosol concentration sustained by vertical transport during rainfall. *Nature* **2016,** *539*, (7629), 416-419.
16. Shilling, J. E.; Pekour, M. S.; Fortner, E. C.; Artaxo, P.; de Sa, S.; Hubbe, J. M.; Longo, K. M.; Machado, L. A. T.; Martin, S. T.; Springston, S. R.; Tomlinson, J.; Wang, J., Aircraft

observations of the chemical composition and aging of aerosol in the Manaus urban plume during GoAmazon 2014/5. *Atmos Chem Phys* **2018,** *18*, (14), 10773-10797.
17. Wang, J.; Pikridas, M.; Spielman, S. R.; Pinterich, T., A fast integrated mobility spectrometer for rapid measurement of sub-micrometer aerosol size distribution, Part I: Design and model evaluation. *J Aerosol Sci* **2017,** *108*, 44-55.
18. Kim, S. *Observations and Modeling of the Green Ocean Amazon 2014/15: hydroxyl radical (OH) chemical ionization mass spectrometer (CIMS) field campaign report, available at https://www.arm.gov/publications/programdocs/doe-sc-arm-15-061.pdf*; University of California, Irvine: 2016.
19. Trebs, I.; Lara, L. L.; Zeri, L. M. M.; Gatti, L. V.; Artaxo, P.; Dlugi, R.; Slanina, J.; Andreae, M. O.; Meixner, F. X., Dry and wet deposition of inorganic nitrogen compounds to a tropical pasture site (Rondonia, Brazil). *Atmos Chem Phys* **2006,** *6*, 447-469.
20. Zaveri, R. A.; Easter, R. C.; Shilling, J. E.; Seinfeld, J. H., Modeling kinetic partitioning of secondary organic aerosol and size distribution dynamics: representing effects of volatility, phase state, and particle-phase reaction. *Atmos Chem Phys* **2014,** *14*, (10), 5153-5181.
21. Zaveri, R. A.; Shilling, J. E.; Zelenyuk, A.; Liu, J. M.; Bell, D. M.; D'Ambro, E. L.; Gaston, C.; Thornton, J. A.; Laskin, A.; Lin, P.; Wilson, J.; Easter, R. C.; Wang, J.; Bertram, A. K.; Martin, S. T.; Seinfeld, J. H.; Worsnop, D. R., Growth Kinetics and Size Distribution Dynamics of Viscous Secondary Organic Aerosol. *Environ Sci Technol* **2018,** *52*, (3), 1191-1199.
22. Zaveri, R. A.; Wang, J.; Fan, J.; Zhang, Y.; Shilling, J. E.; Zelenyuk, A.; Mei, F.; Newsom, R.; Pekour, M.; Tomlinson, J.; Comstock, J. M.; Shrivastava, M.; Fortner, E.; Machado, L. A. T.; Artaxo, P.; Martin, S. T., Rapid growth of air pollution nanoparticles impacts clouds and precipitation in the Amazon rainforest. *under review* **2020**.
23. Kerminen, V. M.; Chen, X. M.; Vakkari, V.; Petaja, T.; Kulmala, M.; Bianchi, F., Atmospheric new particle formation and growth: review of field observations. *Environ Res Lett* **2018,** *13*, (10), 103003.
24. Lee, S. H.; Gordon, H.; Yu, H.; Lehtipalo, K.; Haley, R.; Li, Y. X.; Zhang, R. Y., New Particle Formation in the Atmosphere: From Molecular Clusters to Global Climate. *J Geophys Res-Atmos* **2019,** *124*, (13), 7098-7146.
25. Matsui, H.; Koike, M.; Kondo, Y.; Takegawa, N.; Wiedensohler, A.; Fast, J. D.; Zaveri, R. A., Impact of new particle formation on the concentrations of aerosols and cloud condensation nuclei around Beijing. *J Geophys Res-Atmos* **2011,** *116*, D19208.
26. Cui, Y. Y.; Hodzic, A.; Smith, J. N.; Ortega, J.; Brioude, J.; Matsui, H.; Levin, E. J. T.; Turnipseed, A.; Winkler, P.; de Foy, B., Modeling ultrafine particle growth at a pine forest site influenced by anthropogenic pollution during BEACHON-RoMBAS 2011. *Atmos Chem Phys* **2014,** *14*, (20), 11011-11029.
27. Lupascu, A.; Easter, R.; Zaveri, R.; Shrivastava, M.; Pekour, M.; Tomlinson, J.; Yang, Q.; Matsui, H.; Hodzic, A.; Zhang, Q.; Fast, J. D., Modeling particle nucleation and growth over northern California during the 2010 CARES campaign. *Atmos Chem Phys* **2015,** *15*, (21), 12283-12313.
28. Luo, G.; Yu, F., Simulation of particle formation and number concentration over the Eastern United States with the WRF-Chem plus APM model. *Atmos Chem Phys* **2011,** *11*, (22), 11521-11533.
29. Chen, X. S.; Wang, Z. F.; Li, J.; Yang, W. Y.; Chen, H. S.; Wang, Z.; Hao, J. Q.; Ge, B. Z.; Wang, D. W.; Huang, H. L., Simulation on different response characteristics of aerosol particle

number concentration and mass concentration to emission changes over mainland China. *Sci Total Environ* **2018,** *643*, 692-703.
30. Keskinen, J.; Ronkko, T., Can Real-World Diesel Exhaust Particle Size Distribution be Reproduced in the Laboratory? A Critical Review. *J Air Waste Manage* **2010,** *60*, (10), 1245-1255.
31. Shi, J. P.; Harrison, R. M.; Brear, F., Particle size distribution from a modern heavy duty diesel engine. *Sci Total Environ* **1999,** *235*, (1-3), 305-317.
32. Weimer, S.; Mohr, C.; Richter, R.; Keller, J.; Mohr, M.; Prevot, A. S. H.; Baltensperger, U., Mobile measurements of aerosol number and volume size distributions in an Alpine valley: Influence of traffic versus wood burning. *Atmos Environ* **2009,** *43*, (3), 624-630.
33. Yao, L.; Garmash, O.; Bianchi, F.; Zheng, J.; Yan, C.; Kontkanen, J.; Junninen, H.; Mazon, S. B.; Ehn, M.; Paasonen, P.; Sipila, M.; Wang, M. Y.; Wang, X. K.; Xiao, S.; Chen, H. F.; Lu, Y. Q.; Zhang, B. W.; Wang, D. F.; Fu, Q. Y.; Geng, F. H.; Li, L.; Wang, H. L.; Qiao, L. P.; Yang, X.; Chen, J. M.; Kerminen, V. M.; Petaja, T.; Worsnop, D. R.; Kulmala, M.; Wang, L., Atmospheric new particle formation from sulfuric acid and amines in a Chinese megacity. *Science* **2018,** *361*, (6399), 278-+.
34. Zhao, J.; Smith, J. N.; Eisele, F. L.; Chen, M.; Kuang, C.; McMurry, P. H., Observation of neutral sulfuric acid-amine containing clusters in laboratory and ambient measurements. *Atmos Chem Phys* **2011,** *11*, (21), 10823-10836.
35. Almeida, J.; Schobesberger, S.; Kurten, A.; Ortega, I. K.; Kupiainen-Maatta, O.; Praplan, A. P.; Adamov, A.; Amorim, A.; Bianchi, F.; Breitenlechner, M.; David, A.; Dommen, J.; Donahue, N. M.; Downard, A.; Dunne, E.; Duplissy, J.; Ehrhart, S.; Flagan, R. C.; Franchin, A.; Guida, R.; Hakala, J.; Hansel, A.; Heinritzi, M.; Henschel, H.; Jokinen, T.; Junninen, H.; Kajos, M.; Kangasluoma, J.; Keskinen, H.; Kupc, A.; Kurten, T.; Kvashin, A. N.; Laaksonen, A.; Lehtipalo, K.; Leiminger, M.; Leppa, J.; Loukonen, V.; Makhmutov, V.; Mathot, S.; McGrath, M. J.; Nieminen, T.; Olenius, T.; Onnela, A.; Petaja, T.; Riccobono, F.; Riipinen, I.; Rissanen, M.; Rondo, L.; Ruuskanen, T.; Santos, F. D.; Sarnela, N.; Schallhart, S.; Schnitzhofer, R.; Seinfeld, J. H.; Simon, M.; Sipila, M.; Stozhkov, Y.; Stratmann, F.; Tome, A.; Trostl, J.; Tsagkogeorgas, G.; Vaattovaara, P.; Viisanen, Y.; Virtanen, A.; Vrtala, A.; Wagner, P. E.; Weingartner, E.; Wex, H.; Williamson, C.; Wimmer, D.; Ye, P. L.; Yli-Juuti, T.; Carslaw, K. S.; Kulmala, M.; Curtius, J.; Baltensperger, U.; Worsnop, D. R.; Vehkamaki, H.; Kirkby, J., Molecular understanding of sulphuric acid-amine particle nucleation in the atmosphere. *Nature* **2013,** *502*, (7471), 359-363.
36. Bergman, T.; Laaksonen, A.; Korhonen, H.; Malila, J.; Dunne, E. M.; Mielonen, T.; Lehtinen, K. E. J.; Kuhn, T.; Arola, A.; Kokkola, H., Geographical and diurnal features of amine-enhanced boundary layer nucleation. *J Geophys Res-Atmos* **2015,** *120*, (18), 9606-9624.
37. Yu, F.; Luo, G., Modeling of gaseous methylamines in the global atmosphere: impacts of oxidation and aerosol uptake. *Atmos Chem Phys* **2014,** *14*, (22), 12455-12464.
38. Chen, X. S.; Yang, W. Y.; Wang, Z. F.; Li, J.; Hu, M.; An, J. L.; Wu, Q. Z.; Wang, Z.; Chen, H. S.; Wei, Y.; Du, H. Y.; Wang, D. W., Improving new particle formation simulation by coupling a volatility-basis set (VBS) organic aerosol module in NAQPMS plus APM. *Atmos Environ* **2019,** *204*, 1-11.
39. Scott, C. E.; Rap, A.; Spracklen, D. V.; Forster, P. M.; Carslaw, K. S.; Mann, G. W.; Pringle, K. J.; Kivekas, N.; Kulmala, M.; Lihavainen, H.; Tunved, P., The direct and indirect radiative effects of biogenic secondary organic aerosol. *Atmos Chem Phys* **2014,** *14*, (1), 447-470.
40. Gordon, H.; Sengupta, K.; Rap, A.; Duplissy, J.; Frege, C.; Williamson, C.; Heinritzi, M.; Simon, M.; Yan, C.; Almeida, J.; Trostl, J.; Nieminen, T.; Ortega, I. K.; Wagner, R.; Dunne, E. M.; Adamov, A.; Amorim, A.; Bernhammer, A. K.; Bianchi, F.; Breitenlechner, M.; Brilke, S.;

Chen, X. M.; Craven, J. S.; Dias, A.; Ehrhart, S.; Fischer, L.; Flagan, R. C.; Franchin, A.; Fuchs, C.; Guida, R.; Hakala, J.; Hoyle, C. R.; Jokinen, T.; Junninen, H.; Kangasluoma, J.; Kim, J.; Kirkby, J.; Krapf, M.; Kurten, A.; Laaksonen, A.; Lehtipalo, K.; Makhmutov, V.; Mathot, S.; Molteni, U.; Monks, S. A.; Onnela, A.; Perakyla, O.; Piel, F.; Petaja, T.; Praplanh, A. P.; Pringle, K. J.; Richards, N. A. D.; Rissanen, M. P.; Rondo, L.; Sarnela, N.; Schobesberger, S.; Scott, C. E.; Seinfeldo, J. H.; Sharma, S.; Sipila, M.; Steiner, G.; Stozhkov, Y.; Stratmann, F.; Tome, A.; Virtanen, A.; Vogel, A. L.; Wagner, A. C.; Wagner, P. E.; Weingartner, E.; Wimmer, D.; Winkler, P. M.; Ye, P. L.; Zhang, X.; Hansel, A.; Dommen, J.; Donahue, N. M.; Worsnop, D. R.; Baltensperger, U.; Kulmala, M.; Curtius, J.; Carslaw, K. S., Reduced anthropogenic aerosol radiative forcing caused by biogenic new particle formation. *P Natl Acad Sci USA* **2016,** *113*, (43), 12053-12058.

41. Inomata, S.; Sato, K.; Sakamoto, Y.; Hirokawa, J., Direct observation of new particle formation during ozonolysis of isoprene and ethene competing against the growth of preexisting particles. *Atmos Environ* **2017,** *170*, 149-155.

42. Kiendler-Scharr, A.; Wildt, J.; Dal Maso, M.; Hohaus, T.; Kleist, E.; Mentel, T. F.; Tillmann, R.; Uerlings, R.; Schurr, U.; Wahner, A., New particle formation in forests inhibited by isoprene emissions. *Nature* **2009,** *461*, (7262), 381-384.

43. Lee, S. H.; Uin, J.; Guenther, A. B.; de Gouw, J. A.; Yu, F. Q.; Nadykto, A. B.; Herb, J.; Ng, N. L.; Koss, A.; Brune, W. H.; Baumann, K.; Kanawade, V. P.; Keutsch, F. N.; Nenes, A.; Olsen, K.; Goldstein, A.; Ouyang, Q., Isoprene suppression of new particle formation: Potential mechanisms and implications. *J Geophys Res-Atmos* **2016,** *121*, (24), 14621-14635.

44. Heinritzi, M.; Dada, L.; Simon, M.; Stolzenburg, D.; Wagner, A. C., Molecular understanding of the suppression of new-particle formation by isoprene. *Atmos Chem Phys* **2020,** *20*, 11809–11821.

45. Bonn, B.; Moortgat, G. K., Sesquiterpene ozonolysis: Origin of atmospheric new particle formation from biogenic hydrocarbons. *Geophys Res Lett* **2003,** *30*, (11), 1585.

46. Molteni, U.; Bianchi, F.; Klein, F.; El Haddad, I.; Frege, C.; Rossi, M. J.; Dommen, J.; Baltensperger, U., Formation of highly oxygenated organic molecules from aromatic compounds. *Atmos Chem Phys* **2018,** *18*, (3), 1909-1921.

47. Wang, M. Y.; Chen, D. X.; Xiao, M.; Ye, Q.; Stolzenburg, D.; Hofbauer, V.; Ye, P. L.; Vogel, A. L.; Mauldin, R. L.; Amorim, A.; Baccarini, A.; Baumgartner, B.; Brilke, S.; Dada, L.; Dias, A.; Duplissy, J.; Finkenzeller, H.; Garmash, O.; He, X. C.; Hoyle, C. R.; Kim, C.; Kvashnin, A.; Lehtipalo, K.; Fischer, L.; Molteni, U.; Petaja, T.; Pospisilova, V.; Quelever, L. L. J.; Rissanen, M.; Simon, M.; Tauber, C.; Tome, A.; Wagner, A. C.; Weitz, L.; Volkamer, R.; Winkler, P. M.; Kirkby, J.; Worsnop, D. R.; Kulmala, M.; Baltensperger, U.; Dommen, J.; El Haddad, I.; Donahue, N. M., Photo-oxidation of Aromatic Hydrocarbons Produces Low-Volatility Organic Compounds. *Environ Sci Technol* **2020,** *54*, (13), 7911-7921.

48. Pospisilova, V.; Lopez-Hilfiker, F. D.; Bell, D. M.; El Haddad, I.; Mohr, C.; Huang, W.; Heikkinen, L.; Xiao, M.; Dommen, J.; Prevot, A. S. H.; Baltensperger, U.; Slowik, J. G., On the fate of oxygenated organic molecules in atmospheric aerosol particles. *Sci Adv* **2020,** *6*, (11), eaax8922.

49. Bianchi, F.; Kurten, T.; Riva, M.; Mohr, C.; Rissanen, M. P.; Roldin, P.; Berndt, T.; Crounse, J. D.; Wennberg, P. O.; Mentel, T. F.; Wildt, J.; Junninen, H.; Jokinen, T.; Kulmala, M.; Worsnop, D. R.; Thornton, J. A.; Donahue, N.; Kjaergaard, H. G.; Ehn, M., Highly oxygenated organic molecules (HOM) from gas-phase autoxidation involving peroxy radicals: a key contributor to atmospheric aerosol. *Chem Rev* **2019,** *119*, (6), 3472-3509.

50. Zawadowicz, M. A.; Lee, B.; Shrivastava, M.; Zelenyuk, A.; Zaveri, R. A.; Flynn, C.; Thornton, J. A.; Shilling, J. E., Photolysis Controls Atmospheric Budgets of Biogenic Secondary Organic Aerosol. *Environ Sci Technol* **2020,** *54*, (7), 3861-3870.
51. Kurten, A.; Jokinen, T.; Simon, M.; Sipila, M.; Sarnela, N.; Junninen, H.; Adamov, A.; Almeida, J.; Amorim, A.; Bianchi, F.; Breitenlechner, M.; Dommen, J.; Donahue, N. M.; Duplissy, J.; Ehrhart, S.; Flagan, R. C.; Franchin, A.; Hakala, J.; Hansel, A.; Heinritzi, M.; Hutterli, M.; Kangasluoma, J.; Kirkby, J.; Laaksonen, A.; Lehtipalo, K.; Leiminger, M.; Makhmutov, V.; Mathot, S.; Onnela, A.; Petaja, T.; Praplan, A. P.; Riccobono, F.; Rissanen, M. P.; Rondo, L.; Schobesberger, S.; Seinfeld, J. H.; Steiner, G.; Tome, A.; Trostl, J.; Winkler, P. M.; Williamson, C.; Wimmer, D.; Ye, P. L.; Baltensperger, U.; Carslaw, K. S.; Kulmala, M.; Worsnop, D. R.; Curtius, J., Neutral molecular cluster formation of sulfuric acid-dimethylamine observed in real time under atmospheric conditions. *P Natl Acad Sci USA* **2014,** *111*, (42), 15019-15024.
52. Schobesberger, S.; Junninen, H.; Bianchi, F.; Lonn, G.; Ehn, M.; Lehtipalo, K.; Dommen, J.; Ehrhart, S.; Ortega, I. K.; Franchin, A.; Nieminen, T.; Riccobono, F.; Hutterli, M.; Duplissy, J.; Almeida, J.; Amorim, A.; Breitenlechner, M.; Downard, A. J.; Dunne, E. M.; Flagan, R. C.; Kajos, M.; Keskinen, H.; Kirkby, J.; Kupc, A.; Kurten, A.; Kurten, T.; Laaksonen, A.; Mathot, S.; Onnela, A.; Praplan, A. P.; Rondo, L.; Santos, F. D.; Schallhart, S.; Schnitzhofer, R.; Sipila, M.; Tome, A.; Tsagkogeorgas, G.; Vehkamaki, H.; Wimmer, D.; Baltensperger, U.; Carslaw, K. S.; Curtius, J.; Hansel, A.; Petaja, T.; Kulmala, M.; Donahue, N. M.; Worsnop, D. R., Molecular understanding of atmospheric particle formation from sulfuric acid and large oxidized organic molecules. *P Natl Acad Sci USA* **2013,** *110*, (43), 17223-17228.
53. Ehn, M.; Thornton, J. A.; Kleist, E.; Sipila, M.; Junninen, H.; Pullinen, I.; Springer, M.; Rubach, F.; Tillmann, R.; Lee, B.; Lopez-Hilfiker, F.; Andres, S.; Acir, I. H.; Rissanen, M.; Jokinen, T.; Schobesberger, S.; Kangasluoma, J.; Kontkanen, J.; Nieminen, T.; Kurten, T.; Nielsen, L. B.; Jorgensen, S.; Kjaergaard, H. G.; Canagaratna, M.; Dal Maso, M.; Berndt, T.; Petaja, T.; Wahner, A.; Kerminen, V. M.; Kulmala, M.; Worsnop, D. R.; Wildt, J.; Mentel, T. F., A large source of low-volatility secondary organic aerosol. *Nature* **2014,** *506*, (7489), 476-479.
54. Sarnela, N.; Jokinen, T.; Duplissy, J.; Yan, C.; Nieminen, T.; Ehn, M.; Schobesberger, S.; Heinritzi, M.; Ehrhart, S.; Lehtipalo, K.; Trostl, J.; Simon, M.; Kurten, A.; Leiminger, M.; Lawler, M. J.; Rissanen, M. P.; Bianchi, F.; Praplan, A. P.; Hakala, J.; Amorim, A.; Gonin, M.; Hansel, A.; Kirkby, J.; Dommen, J.; Curtius, J.; Smith, J. N.; Petaja, T.; Worsnop, D. R.; Kulmala, M.; Donahue, N. M.; Sipila, M., Measurement-model comparison of stabilized Criegee intermediate and highly oxygenated molecule production in the CLOUD chamber. *Atmos Chem Phys* **2018,** *18*, (4), 2363-2380.
55. Berndt, T.; Richters, S.; Jokinen, T.; Hyttinen, N.; Kurten, T.; Otkjaer, R. V.; Kjaergaard, H. G.; Stratmann, F.; Herrmann, H.; Sipila, M.; Kulmala, M.; Ehn, M., Hydroxyl radical-induced formation of highly oxidized organic compounds. *Nat Commun* **2016,** *7*, 13677.
56. Shilling, J. E.; Chen, Q.; King, S. M.; Rosenoern, T.; Kroll, J. H.; Worsnop, D. R.; McKinney, K. A.; Martin, S. T., Particle mass yield in secondary organic aerosol formed by the dark ozonolysis of alpha-pinene. *Atmos Chem Phys* **2008,** *8*, (7), 2073-2088.
57. Presto, A. A.; Donahue, N. M., Investigation of alpha-pinene plus ozone secondary organic aerosol formation at low total aerosol mass. *Environ Sci Technol* **2006,** *40*, (11), 3536-3543.
58. Ng, N. L.; Chhabra, P. S.; Chan, A. W. H.; Surratt, J. D.; Kroll, J. H.; Kwan, A. J.; McCabe, D. C.; Wennberg, P. O.; Sorooshian, A.; Murphy, S. M.; Dalleska, N. F.; Flagan, R. C.; Seinfeld, J. H., Effect of NOx level on secondary organic aerosol (SOA) formation from the photooxidation of terpenes. *Atmos Chem Phys* **2007,** *7*, (19), 5159-5174.

59. Yu, F.; Luo, G.; Pryor, S. C.; Pillai, P. R.; Lee, S. H.; Ortega, J.; Schwab, J. J.; Hallar, A. G.; Leaitch, W. R.; Aneja, V. P.; Smith, J. N.; Walker, J. T.; Hogrefe, O.; Demerjian, K. L., Spring and summer contrast in new particle formation over nine forest areas in North America. *Atmos Chem Phys* **2015,** *15*, (24), 13993-14003.
60. Chen, X. S.; Wang, Z. F.; Li, J.; Chen, H. S.; Hu, M.; Yang, W. Y.; Wang, Z.; Ge, B. Z.; Wang, D. W., Explaining the spatiotemporal variation of fine particle number concentrations over Beijing and surrounding areas in an air quality model with aerosol microphysics. *Environ Pollut* **2017,** *231*, 1302-1313.
61. Elleman, R. A.; Covert, D. S., Aerosol size distribution modeling with the Community Multiscale Air Quality modeling system in the Pacific Northwest: 3. Size distribution of particles emitted into a mesoscale model. *J Geophys Res-Atmos* **2010,** *115*, D03204.